Air-Conditioning
and Refrigeration
Technology Institute

Final Report

ARTI Report No. 07010-01

PARTICLE IMAGE VELOCIMETRY MEASUREMENTS AND CFD-BASED PREDICTIONS OF AIR DISTRIBUTION AT EVAPORATOR INLET AND OUTLET

Final Report

Date Published – August 2009

David A. Yashar and Piotr A. Domanski

THE NATIONAL INSTITUTE OF STANDARDS AND TECHNOLOGY
100 Bureau Drive, Mailstop 8631
Gaithersburg, MD 20899-8631

Prepared for

AIR-CONDITIONING AND REFRIGERATION TECHNOLOGY INSTITUTE, INC
2111 Wilson Boulevard, Suite 500, Arlington, Virginia 22201-3001

DISCLAIMER

This report was prepared as an account of work sponsored by the Air-Conditioning and Refrigeration Technology Institute, Inc. (ARTI). Neither ARTI, its research program financial supporters, or any agency thereof, nor any of their employees, contractors, subcontractors or employees thereof - makes any warranty, expressed or implied; assumes any legal liability or responsibility for the accuracy, completeness, any third party's use of, or the results of such use of any information, apparatus, product, or process disclosed in this report; or represents that its use would not infringe privately owned rights. Reference herein to any specific commercial product, process, or service by trade name, trademark, manufacturer, or otherwise, does not necessarily constitute nor imply its endorsement, recommendation, or favoring by ARTI, its sponsors, or any agency thereof or their contractors or subcontractors. The views and opinions of authors expressed herein do not necessarily state or reflect those of ARTI, its program sponsors, or any agency thereof.

Funding for this project was provided by (listed alphabetically):
- Air-Conditioning, Heating and Refrigeration Institute (AHRI)
- Copper Development Association (CDA)
- Heating, Refrigeration and Air Conditioning Institute of Canada (HRAI)
- New York State Energy Research and Development Authority (NYSERDA)

PARTICLE IMAGE VELOCIMETRY MEASUREMENTS AND CFD-BASED PREDICTIONS OF AIR DISTRIBUTION AT EVAPORATOR INLET AND OUTLET

David A. Yashar and Piotr A. Domanski
National Institute of Standards and Technology
Gaithersburg, MD 20899

Abstract

We examined the air flow distribution through a residential indoor air conditioning heat exchanger. The test heat exchanger was a finned tube, A-shaped coil outfitted with a condensation collection pan required for a horizontal installation configuration. We examined the air flow distribution approaching and exiting the coil at two different air flow rates and two humidity levels. Our dry coil PIV measurements indicate that the presence of the condensation collection pan impedes air flow through the lower slab of the coil causing approximately 20 % more air flow through the upper slab than the lower slab. Also, the measurements uncovered some portions of the coil where the flow is blocked by the mounting brackets. The wet coil tests showed that the presence of water on the surface of the coil causes a large increase in the resistance to air flow through the coil, but the water concentration was not uniformly dispersed throughout the coil. The air flow distribution was not largely affected by the overall flow rate of air, except in the wet coil tests where the water concentration on the coil changed with air velocity. We also developed a CFD model of the flow through the test coil, based on a momentum resistance modeling approach. For the cases studied, the CFD results matched approximately 90 % of the measured data within 15 % for the upper slab and 20 % for the lower slab of the coil.

Keywords: Air Flow Distribution, Residential Air Conditioning Coil, Particle Image Velocimetry (PIV), Computational Fluid Dynamics (CFD)

Acknowledgement

This work was sponsored in part by the Air-conditioning and Refrigeration Technology Institute (ARTI) under contract number ARTI-07010. We acknowledge all of the comments and support from the members of the ARTI-07010 Project Monitoring Subcommittee. Dr. W. Vance Payne contributed to the test apparatus design, operation, and data acquisition. Mr. John Wamsley provided technician support during the construction phase of this project. Dr. Rodney Bryant assisted us through his knowledge of Particle Image Velocimetry measurement techniques. Mr. Michael Galler also provided helpful input by commenting on the draft of this report.

Table of Contents

List of Figures

Nomenclature

A	Area	m^2
C_l	Linear Momentum Resistance Combined Coefficient	$kg\ s^{-1}\ m^3$
C_p	Specific Heat	$m^2\ s^{-2}\ K^{-1}$
C_q	Quadratic Momentum Resistance Combined Coefficient	$kg\ m^4$
K_l	Linear Momentum Resistance Coefficient	s^{-1}
K_q	Quadratic Momentum Resistance Coefficient	m^{-1}
$\dot{m}$	Mass Flow Rate	$kg\ s^{-1}$
P	Pressure	$N\ m^{-2}$
Q	Heat Transfer Rate	W
R	Universal Gas Constant	$J\ kg^{-1}\ K^{-1}$
T	Temperature	ºC
u	x-directional velocity	$m\ s^{-1}$
V	Velocity	$m\ s^{-1}$
$\dot{\forall}$	Volumetric Flow Rate	$m^3\ s^{-1}$
x	Distance along HX surface	m

Greek Symbols

β	Porosity	none
ρ	Density	$kg\ m^{-3}$
ω	Humidity Ratio	none

1. INTRODUCTION

Finned tube heat exchangers are the predominant type of heat exchangers used in comfort cooling applications. Finned-tube heat exchangers are generally made up of a bundle of several dozen tubes, each of which is an individual cross flow heat exchanger. The performance of the heat exchanger as a whole is therefore the aggregate performance of every tube in the bundle. The heat exchange performance of each individual tube is influenced by many parameters, one of the most important being the velocity or quantity of air that it has available for heat exchange. To this end, the distribution of the air incident on the heat exchanger has a profound impact on its overall performance, since this parameter governs the velocity of air at each tube location in the bundle.

Chwalowski et al. (1989) have shown that the air flow distribution in residential applications is far from uniform; Payne et al. (2003) demonstrated that air-side non-uniformity imposes a reduction in heat exchanger capacity, which can be as much as 30% in the extreme cases. Unfortunately, the problem of air-side velocity distribution is not well addressed because adequate tools needed to address it have not been available to design engineers. Consequently, there is a tendency to assume a uniform air velocity profile or implement a refrigerant circuitry that would offer some degree of robustness with non-uniform air distribution. The current state-of-the-art is to measure air-side velocity distribution by traversing a hot wire anemometer or pitot tube. Although these methods are simple and low cost, they are cumbersome and have high measurement uncertainty. One of the major drawbacks of these tools is that their accuracy is limited by the user's ability to maintain the position and orientation of the sensor in the exact location of interest. Furthermore, the probes for these tools are obstructive to the flow field. There are a few optically based methods available, which eliminate disruptions of the flow by the sensor probe, specifically Laser Doppler Anemometry (LDA) and Particle Image Velocimetry (PIV). While very accurate, LDA can be used to measure the flow at a single point, and would therefore be quite cumbersome to use as a method to characterize air flow through a heat exchanger. PIV is the focus of this study since it provides the ability to characterize large sections of the flow field.

A study by Domanski et al. (2004), involving our recent developments in machine learning as incorporated into the Intelligent System for Heat Exchanger Design (ISHED), has demonstrated that the majority of the capacity degradation due to air-side non-uniformity can be eliminated by designing the optimal refrigerant circuitry for the actual air flow distribution. This study demonstrated that the capacity of a heat exchanger operating with a highly non-uniform air flow distribution can be improved by as much as 10 % if knowledge of the air distribution is applied to the refrigerant circuitry design. Therefore, knowledge of the air-side velocity distribution is crucial for designing high-performance heat exchangers.

Preliminary measurements on three finned-tube heat exchangers by Yashar and Cho (2007) demonstrated that PIV can uncover detailed air flow patterns that cannot be registered by traditional measurement methods. Concurrently, we worked on developing CFD models to match the measured air flow distributions. The goal of the present study is to use PIV to make high-accuracy measurements and validate CFD-based models for high-accuracy predictions of air velocity profiles for a residential air-conditioning coil. The present study is based upon a two-slab finned tube indoor heat exchanger. The study examines how the air flow distribution differs when operating at the rated and reduced air flow rate, and how the air flow distribution is affected by water condensing on the heat exchanger surface.

2. EXPERIMENTAL SETUP

2.1 Test Coil

2.1.1 Coil Description

The test coil used in this study was a 3-ton residential air-conditioning, finned-tube heat exchanger shown in Figure 2.1. It consisted of two heat exchanger slabs configured in the A-shape with an apex angle of 40 degrees. Each slab was made up of 60 tubes located in three depth rows with wavy fins. The tubes had an outside diameter of 9.5 mm (3/8 inch) and were spaced 25.4 mm (1 inch) apart along the height of the heat exchanger. The depth rows were layered in a staggered configuration and were spaced 19 mm (3/4 inch) apart. The overall dimensions of each slab were 508 mm (20 inch) tall, 457 mm (18 inch) wide, and 57.2 mm (2 ¼ inch) thick.

The heat exchanger was installed in the horizontal flow configuration, with a condensation collection device comprised of two parts. The first part was a plastic tray that locked onto the lower section of the coil's mounting bracket at the base of the heat exchanger; the second part was a metal sheet that clipped into the plastic tray. Figure 2.1 shows the coil assembly in the upward position prior to installation. When installed horizontally in the test section, the condensation collection device was located underneath the coil where it would catch water running off of the coil.

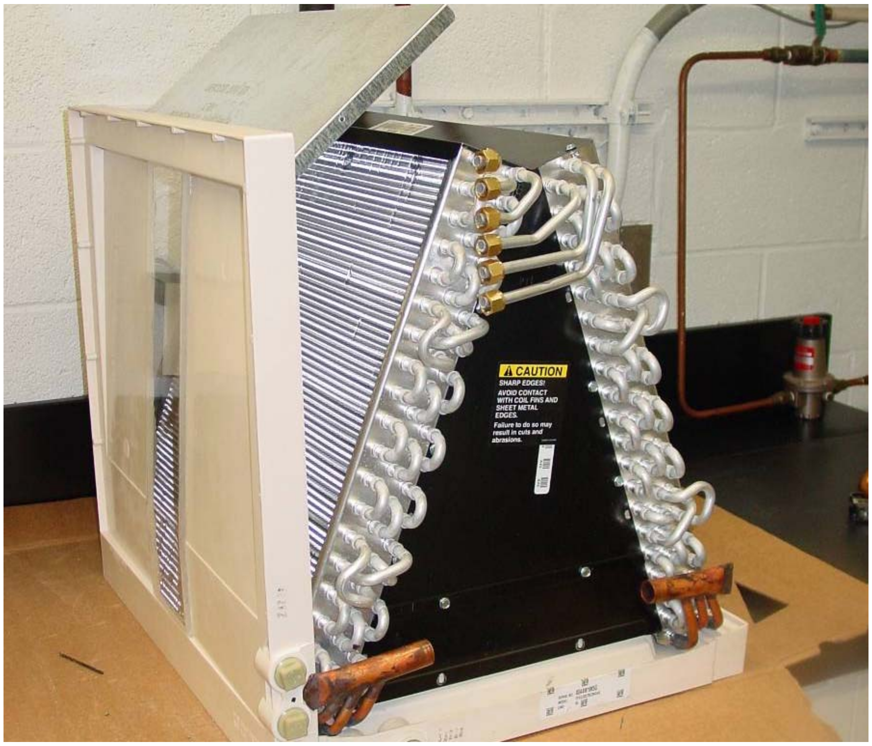

Figure 2.1 Test coil

It is important to note the geometry of the plastic mounting bracket attached to the base of the test coil. This mounting bracket holds the coil position in the duct and it maintains the angle between the two slabs. It would also act as a condensation runoff conduit if the coil were positioned in the upflow configuration with the base positioned at the bottom and the apex at the top. Its design is such that it overlaps the bottom of the inlet surface of the coil on both slabs, effectively sealing off the inlet of this region, which is indicated by the ellipse in Figure 2.2. The inner lip of the mounting bracket overlaps the bottom 45 mm (1 ¾ inch) of the heat exchanger.

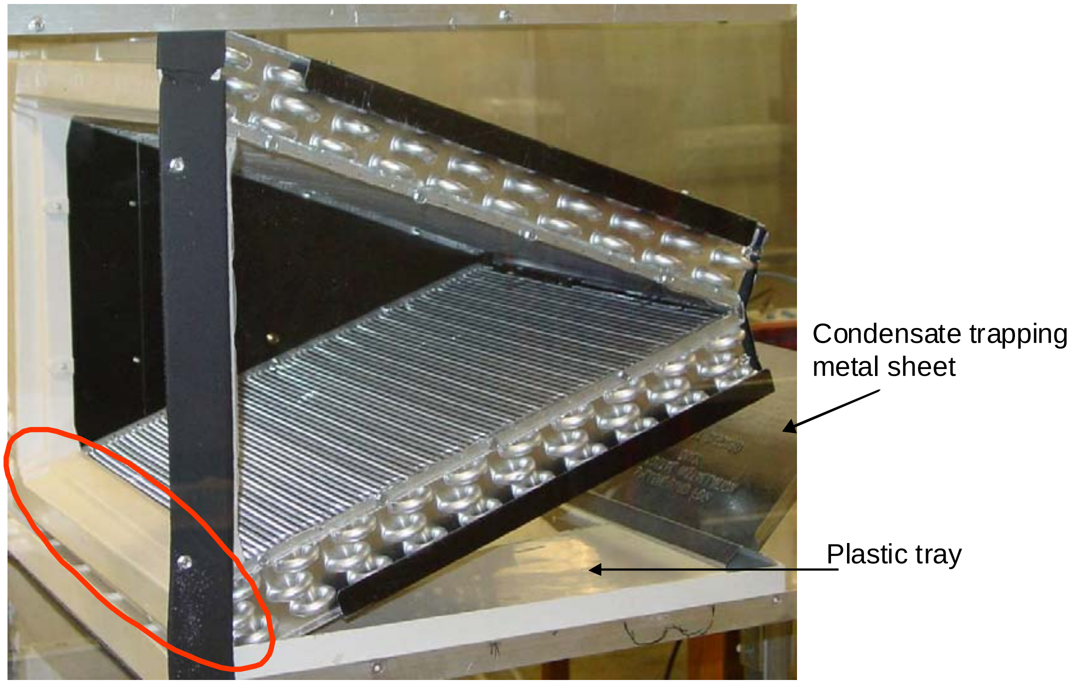

Figure 2.2 Test coil with emphasis on inner lip of mounting bracket

2.1.2 Coil Modifications

We modified three aspects of the test coil for the purpose of experimentation. The first modification was to the condensation collection tray. We made a window to provide visual access to the exit side of the lower slab by cutting out a small section of the plastic tray and replacing it with clear plexiglass (visible in Figure 2.1).

The second modification that we made was to the refrigerant side headers that were connected to the inlet and exit tubes of the heat exchanger. In normal field use, the refrigerant would flow through an expansion device and through a distributor that divided the flow amongst six small diameter tubes, each routing a portion of the flow to one of the six inlet tubes. We replaced the small diameter tubes with larger ones since our experiment was designed to circulate cold water through the heat exchanger. We merged the new tubes near the base of each heat exchanger slab into their own header.

The third modification was that we reversed the flow of the fluid through the heat exchanger since this allowed individual measurement of the heat exchange provided by each slab of the coil by the water enthalpy method. A typical installation of this coil would route the refrigerant through one of the six circuits entering at the coil's base and flowing to the apex where the six circuits are merged in a header. In this laboratory study, we delivered cold water to the header at the coil's apex, where it was split between the six circuits, and then flowed towards the coil's base. A schematic of the test coil outlining the water flow direction is shown in Figure 2.3.

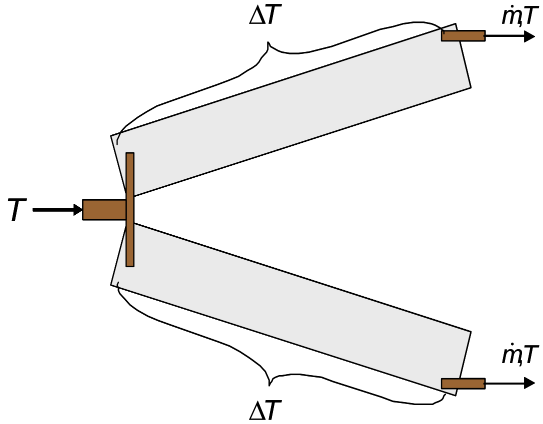

Figure 2.3 Test coil water flow direction

2.2 Test Apparatus

The test apparatus consisted of three components, an air flow loop, a chilled water flow loop, and a PIV air flow measurement system. The entire apparatus was housed in an environmental chamber capable of maintaining the laboratory air conditions between 10 ºC and 60 ºC dry bulb and relative humidity within 2 % of the target setpoint.

2.2.1 Air Flow Loop and Water Flow Loop

A schematic of the air flow loop and the water flow loop is shown in Figure 2.4. The air flow loop consisted of the test section and an air flow measurement and control section. The test section was a plexiglass duct, 2438 mm (8 feet) long, 521 mm (20 ½ inch) tall, and 565 mm (22 ¼ inch) wide, which was constructed around the test coil. Air entered the test section, flowed through the test coil, and then out towards the air flow measurement and control section (shown as left to right in Figure 2.4). The test section was constructed out of clear plexiglass so that we could visually observe the test coil during operation. In the measurement and control section, the air flowed through a nozzle where the flow rate was measured according to ASHRAE Standard 37, then through a blower powered by a variable-speed motor. In this fashion, we could measure and control the flow rate of air through the test section.

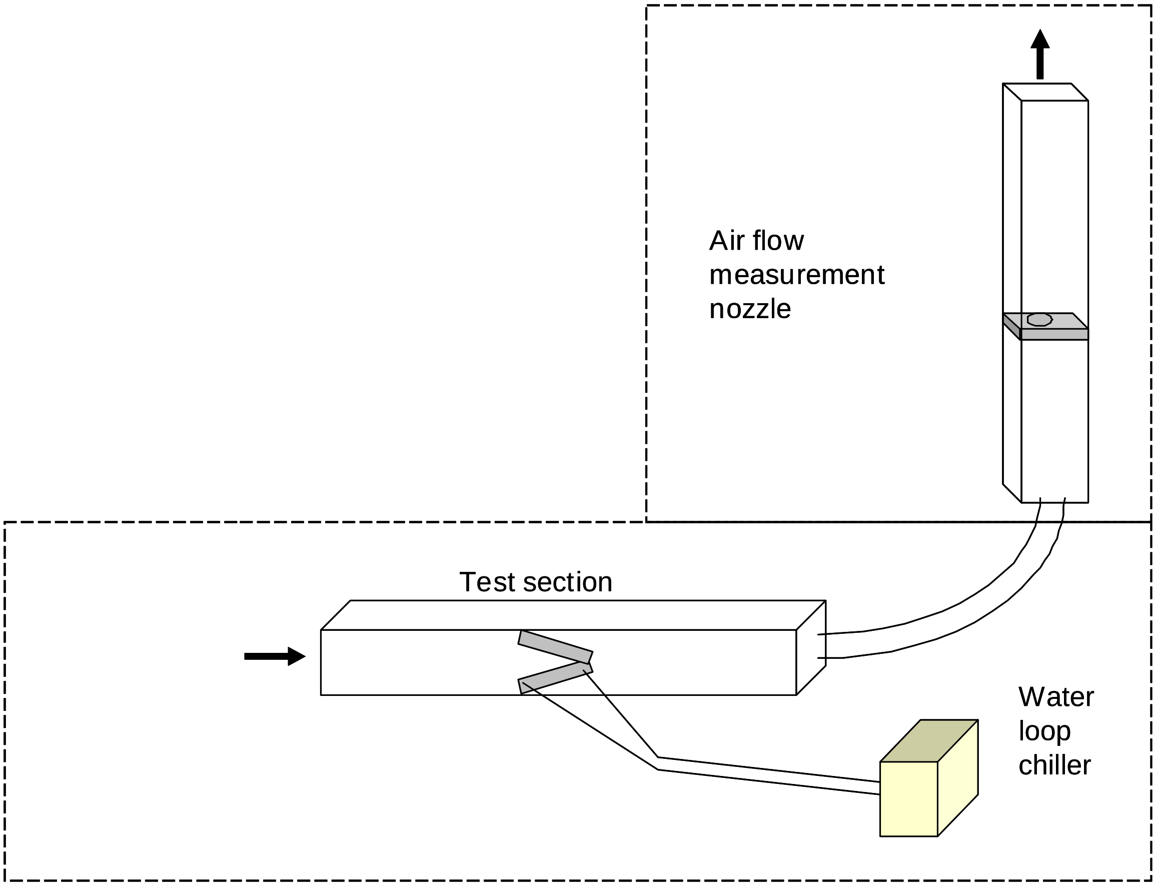

Figure 2.4 Air flow loop and water flow loop

We circulated chilled water through the test coil in the test section using a portable chiller. The chiller was capable of delivering up to 1.4 l/s (22 GPM) of water at a constant temperature by removing up to 24 kW (82 kBtu/h) of heat. We measured the temperature of the water entering and exiting each slab of the test coil using T-type thermocouples calibrated to 0.15 ºC. We also measured the temperature difference between the water entering and exiting each slab using 5 junction thermopiles calibrated to 0.10 ºC. All temperature probes were inserted into oil filled reservoirs that were immersed in the flow entering and leaving each header, as shown in Figure 2.5. We measured the flow rate of water for each slab downstream of the test coil using inline flow meters, and balanced the flow between the slabs using downstream valves so that each slab received the same flow rate of water. The water that passed through the top slab of the heat exchanger was routed through a coriolis-type flow meter, calibrated to 0.03 g/s (0.24 lb/h), to accurately measure the flow rate before entering the inline flow meter. After measuring the water flow rate through each slab, the water was returned to the portable chiller. This configuration enabled us to calculate the heat transferred to each slab of the heat exchanger from the thermodynamic properties of the water, the temperature difference, and the flow rate.

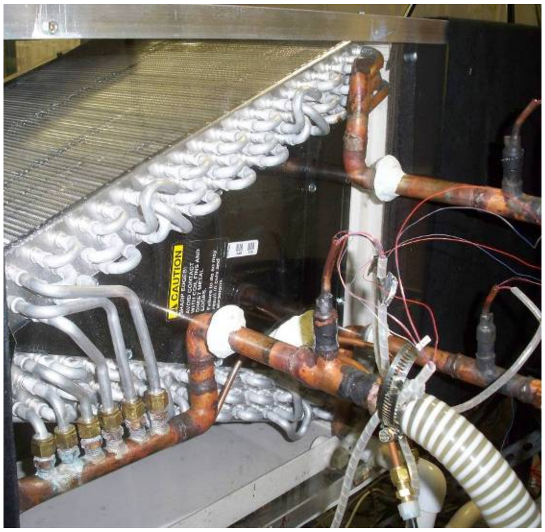

Figure 2.5 Thermocouple and thermopile placement on test coil

2.2.2 PIV Air Flow Measurement System

PIV works on the basis of tracking the motion of “seed” particles entrained in the flow field. The seed particles act as markers within the flow field whose displacement can be mapped between two points in time. As the seed particles move through the test section they are illuminated by a series of laser light sheets. The laser sheets are oriented in such a way that the illuminated plane is aligned to the main flow direction within the test section; therefore particles moving downstream will remain within this plane. A camera is used to capture images within this plane and therefore records the distance traveled by the seed particles over a fixed length of time, which allows us to extract the velocity. Figure 2.6 shows a schematic of a basic 2D PIV setup.

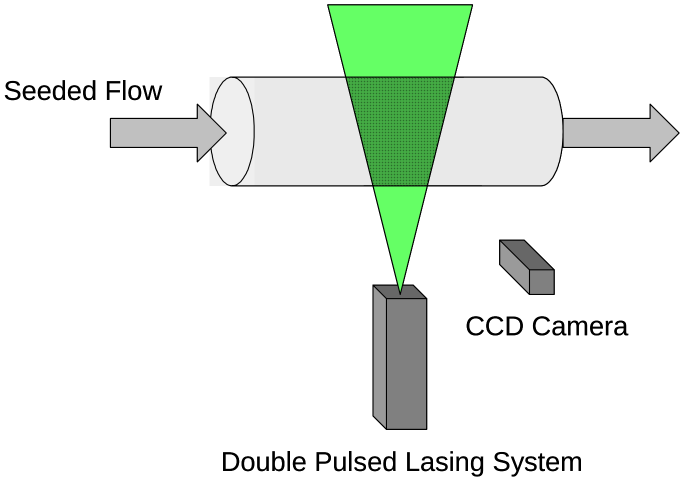

Figure 2.6 Schematic of 2-dimensional PIV setup

The PIV measurement system consisted of a pair of Class IV pulsed lasers outfitted with a sheet forming optical lens, a double framed Charged Coupled Device camera, a theater style fog generator, and a Programmable Timing Unit (PTU) controlled by personal computer. For safety purposes, we covered the entire test section with heavy black material to contain the reflections of scattered laser light. A detailed description of the measurement equipment can be found in Yashar and Cho (2007). Appendix A contains the uncertainty analysis for the PIV measurements.

2.3 PIV Data Collection Method

The location of the measurement equipment relative to the test section varied for different measurements. Figure 2.7 shows the setup for measurements on air flow approaching the inlet of the test coil. In this configuration, the lasers are positioned in front of the test section inlet, so that the light sheet is projected onto the inlet surface of the coil. The camera is located to the side of the test section, facing the illuminated plane that intersects the inlet surface of the coil. The operation of the camera and the lasers are synchronized by the PTU, and data is reduced by mapping the motion of fog particles within the illuminated plane between successive laser pulses.

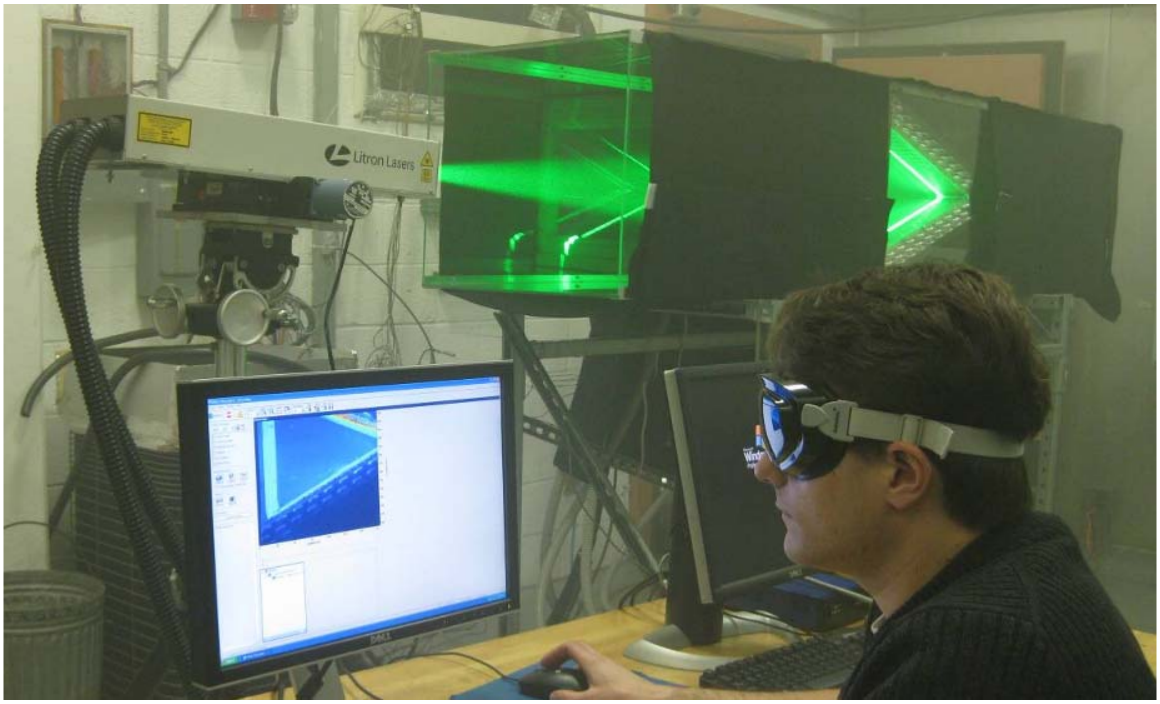

Figure 2.7 PIV data collection for inlet air velocity profile

Figure 2.8(a) and (b) illustrate the placement of the PIV equipment for measuring the air flow velocity profile exiting the test coil. Here, the laser light sheet is projected horizontally towards the exit surface of the coil, and the camera is positioned underneath the test section looking upwards.

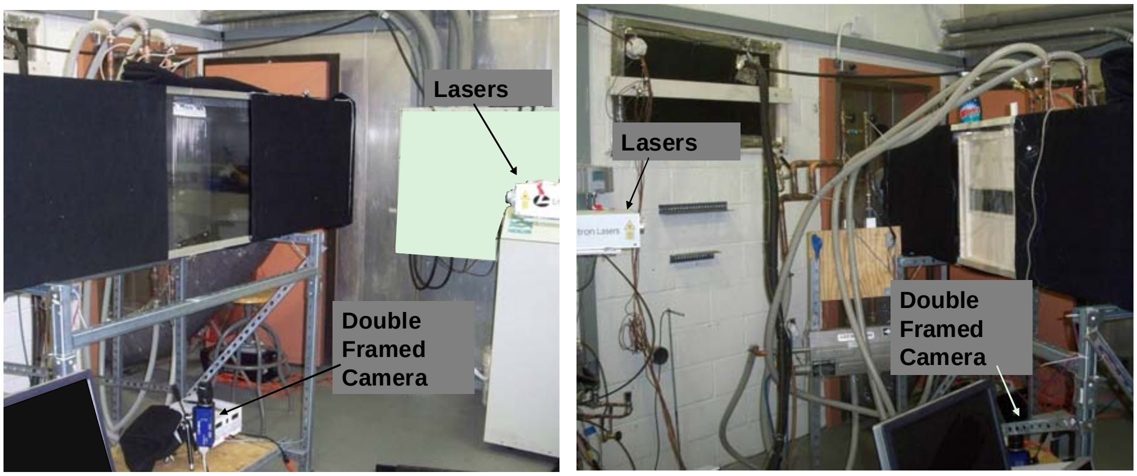

(a) (b)

Figure 2.8 Measurement setup for (a) upper slab and (b) lower slab

We aligned and calibrated the PIV system prior to every measured data set in order to measure the air flow profile at the specific measurement location. The process began by aligning the lasers into position at the lateral center of the test coil. Alignment was performed by placing a laminated sheet of yellow paper on the coil surface so that a straight line on the paper was aligned with the desired laser light sheet position. The reflection of the 532 nm laser light from a yellow surface is visible through laser safety glasses. The lasers were mounted on top of a traversing platform with two axis rotation and could be moved from a remote location. Once the laser light was roughly aligned to the mark on the yellow paper, the laser was turned on at low power and the position was adjusted until the light sheet overlaid the alignment mark. The alignment process is shown in Figure 2.9.

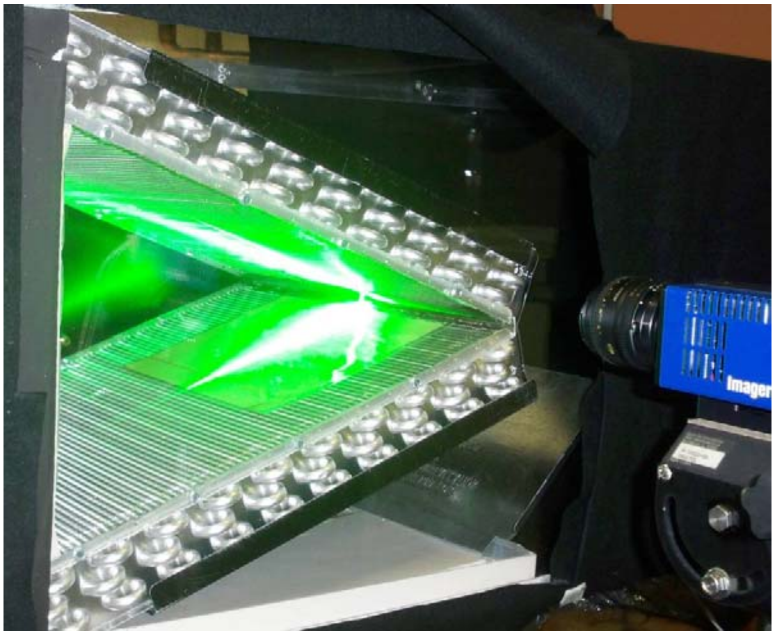

Figure 2.9 Alignment of laser to measurement plane

After the laser was aligned, the camera was calibrated to the image plane by taking a photograph of a ruler positioned in the image plane. Figure 2.10 depicts a typical calibration process. After obtaining a photograph of the ruler in the image plane, scaling marks were tagged to the image and the true distance between them was used to calibrate the data set.

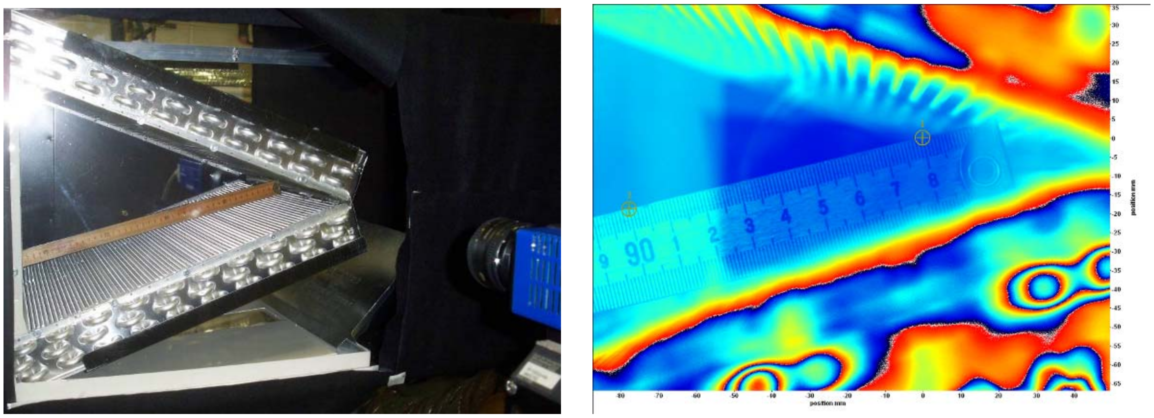

Figure 2.10 (a) Calibration process (b) Calibration photograph

We acquired each data set once the alignment and calibration was completed. We began this process by filling the entire laboratory with glycerin-based theater fog, which served as seed particles for the PIV measurements. We then captured a series of image pairs of the seeded air flow in the measurement area. Each image pair consisted of two pictures separated in time by (160 to 750) μs, depending on the data set. Successive image pairs were taken every 67 ms. We calculated the velocity field from the motion of the particles from an image to its paired image, which resulted in a series of time elapsed vector fields. We then averaged these vector fields to dilute the unsteady components of the turbulent flow structures and produce a more steady-state representation of the flow field. Figure 2.11 shows a snapshot of some of PIV measurements of the air flow approaching an A-shaped finned-tube heat exchanger. The coil is positioned on its side and the air-flow is left-to-right; Figure 2.11 (a) shows a camera image of an illuminated plane of seed particles; Figure 2.11 (b) shows the computed velocity vector field.

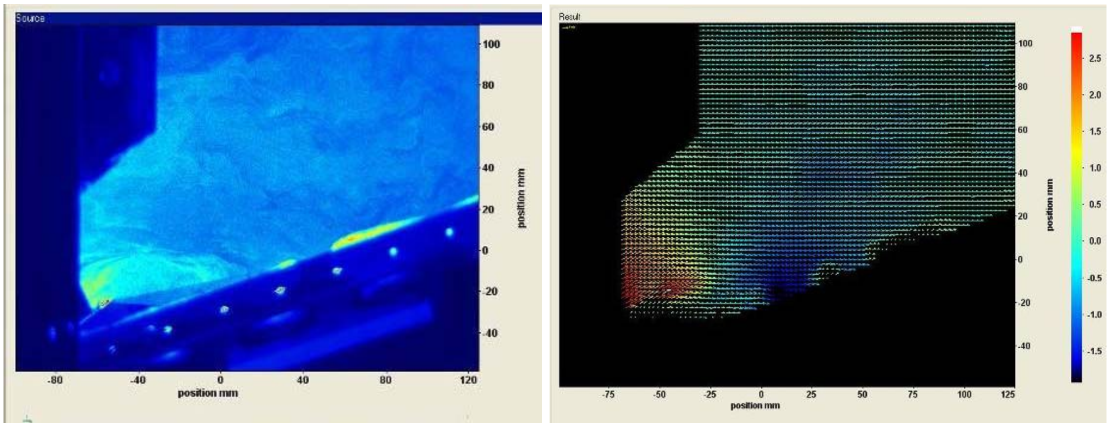

(a) (b)

Figure 2.11 Air flow approaching bottom slab of an A-shaped coil

We characterized each test case by measuring the entire surface in sections and then assembled the data from these sections to form complete data sets. The alignment and calibration process was performed prior to each scan and each calibration set was unique to each scan.

2.4 Test Matrix

The test matrix is presented in Table 2.1. It was designed to encompass both inlet and out flow velocity profiles, examine the effects of air flow rate variation and the effects of condensation on the coil. The constant parameters for all tests were the inlet air dry bulb temperature of 26.7 ºC (80 ºF) and the inlet water temperature of 7.2 ºC (45 ºF). The baseline test case for this study represents the test coil operating under design conditions, with the rated air flow rate of 0.566 m^3s^{-1} (1200 CFM) at 26.7 ºC (80 ºF) dry bulb temperature and the humidity low enough to prevent condensation on the coil surface.

Table 2.1 PIV Measurement Test Matrix

Test	HX Slab	HX Face	Air Flow Rate	Inlet Air Dew Point
1a	Upper	Inlet	0.566 m^3s^{-1} (1200 CFM)	<7.0 ºC (44.6 ºF)
1b	Lower	Inlet		
1c	Upper	Outlet		
1d	Lower	Outlet		
2a	Upper	Inlet	0.425 m^3s^{-1} (900 CFM)	<7.0 ºC (44.6 ºF)
2b	Lower	Inlet		
3a	Upper	Inlet	0.566 m^3s^{-1} (1200 CFM)	15.9 ºC (60.7 ºF)
3b	Lower	Inlet		
4a	Upper	Inlet	0.425 m^3s^{-1} (900 CFM)	15.9 ºC (60.7 ºF)
4b	Lower	Inlet		

3. PIV MEASUREMENTS

3.1 Baseline Tests (1a, 1b, 1c, and 1d)

Inlet and Exit Velocity Measurements for 0.566 m^3s^{-1} *(1200 CFM) Dry Coil Tests*

The baseline test case is that of the manufacturer's specified air flow rate and dry coil conditions. We operated the test section with the target test conditions listed in the test matrix; the time averaged measured values throughout the duration of the tests are shown below (the uncertainty analysis for these data are presented in Appendix A):

- Volumetric flow rate of air: 0.563 m^3s^{-1} (1194 CFM)
- Air entering dry bulb temperature: 27.0 ºC (80.6 ºF)
- Air entering dew point temperature: 4.2 ºC (39.5 ºF), 23% RH
- Water inlet temperature: 7.0 ºC (44.7 ºF)
- Water mass flow rate: 285 gs^{-1} per slab

The temperature increase of the water flowing through the heat exchanger was 4.6 ºC (8.3 ºF) for the upper slab and 3.8 ºC (6.8 ºF) for the lower slab. Based on these measurements, we calculated the total heat transfer to be 9.91 kW, of which 5.44 kW was transferred through the top slab and 4.47 kW was transferred through the bottom slab; a difference of 22%. These basic measurements indicated that there is a significant difference in the amount of air flowing through the two slabs of the heat exchanger. The presence of the condensation collection device effectively increases the flow resistance for the air that passes through the lower slab; therefore, some air flow is routed away from the lower portion of the test section and passes through the upper slab. This was confirmed by the PIV measurements; numerical integration of the PIV data showed that 17.9 % more air passed through the upper slab than the lower slab.

The PIV measurements for the approach air flow to the upper and lower slabs of this coil are shown in Figure 3.1. The data is plotted as the component of the velocity vectors perpendicular to the surface of the coil. The horizontal axis shows the position along the coil, with zero being the base of the coil and the upper end at the apex. The data for both slabs show a generally similar pattern. First, the bottom most 50 mm – 60 mm (2" to 2 3/8") of the heat exchanger receives no air flow because the mounting bracket blocks off this portion of the heat exchanger's inlet surface. At a certain point afterwards, there is a spike in the amount of air flow incident on the coil. This region is shown at approximately 65 mm – 100 mm (2 1/2" to 4") on the figure. It is also of interest to note the rapid drop off of air flow near the apex.

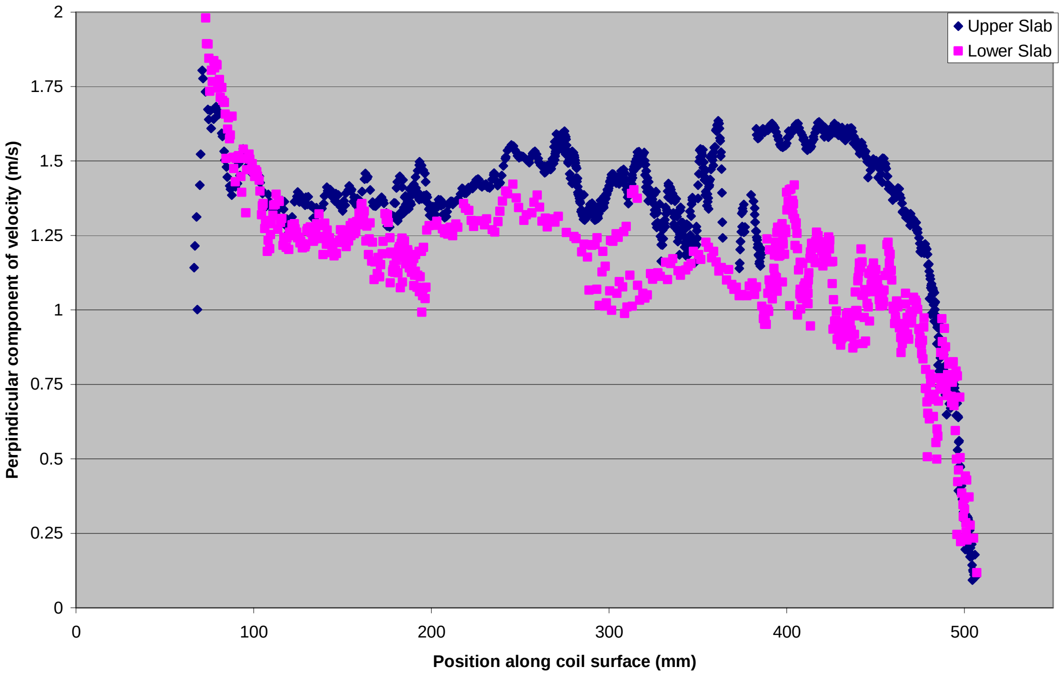

Figure 3.1 Velocity profiles for inlet to dry coil at 1200 CFM, Tests 1a and 1b

Tracking the motion of particles entering and leaving the test coil uncovers a lot of detail regarding the local flow patterns. In particular, the velocity profile displays a sinusoidal pattern that corresponds to the presence and absence of a tube in the first depth row. As the air gets closer and closer to the coil, the streamlines will converge towards locations which are gaps between tubes in the first depth row. This causes the approach velocity profile to form a periodic set of velocity peaks and valleys. The magnitude of this sinusoidal component is relatively small at some distance from the inlet side of the heat exchanger, but it is noticeably large on many of the PIV measurements if the images were taken very close to the coil. On the exit side of the coil, air leaves the heat exchanger entirely through the gaps between successive tubes in the last depth row, and there are no features in the flow field to change this pattern. Therefore, the PIV data taken at the exit side of the coil shows a very large sinusoidal component. Figure 3.2 shows a PIV photograph of the coil exit with the reduced vector data overlaid onto the photograph. This effect was clearly present on all PIV measured data at the coil outlet.

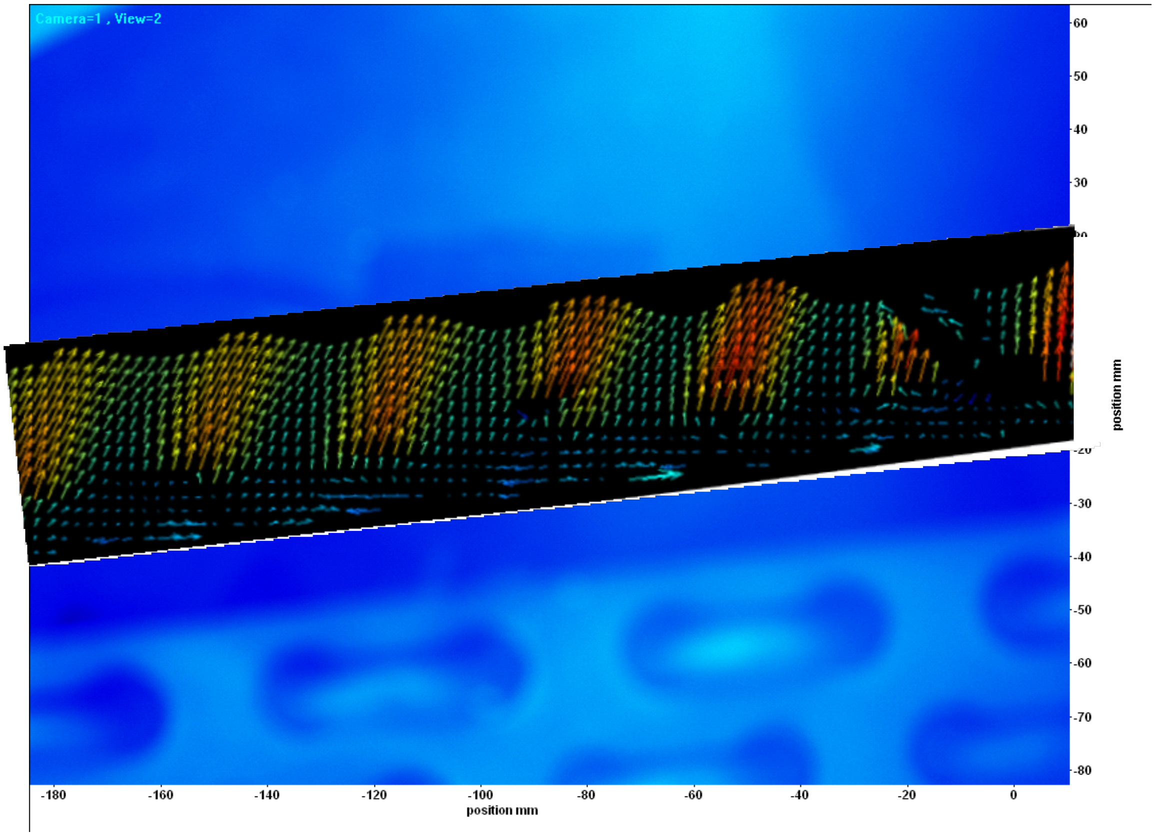

Figure 3.2 PIV velocity field at the upper slab exit, dry coil at 1200 CFM, Test 1c

Figure 3.3 shows the PIV measurements for the exit air flow from the upper slab of the test coil. Again the data is plotted as the perpendicular component of velocity versus the position along the coil surface. The uncertainty for this data set is approximately 3 % at 95 % confidence. The left hand side (coil position zero) represents the portion closest to the base and the right hand side of the graph represents the coil apex. It was difficult to acquire PIV data in the portion nearest to the coil base because this section was very close to the duct wall and its view was partially obstructed by the rails holding the ductwork together. At first sight it is a little difficult to see the general pattern, since the sinusoidal component is very large. Upon close examination, it appears that the flow is increasing rapidly with position for the first 150 mm (6”) or so; then is much flatter, but still increasing with position until it gets close to the end of the coil.

Figure 3.4 shows the PIV measurements for the exit air flow from the lower slab of the test coil. The measurement uncertainty for this data set is better than 3 % at 95 % confidence. This data was difficult to collect because the condensation collection device obstructed the view to some portions of the exit of the lower slab. Also, the data in the 150 mm to 250 mm (6” to 10”) region was corrupted by scattered reflections, so this small section of the data is not reliable. However, the general pattern is obvious from this data, and it is similar to that of the air leaving the upper slab; but the velocity magnitude is smaller.

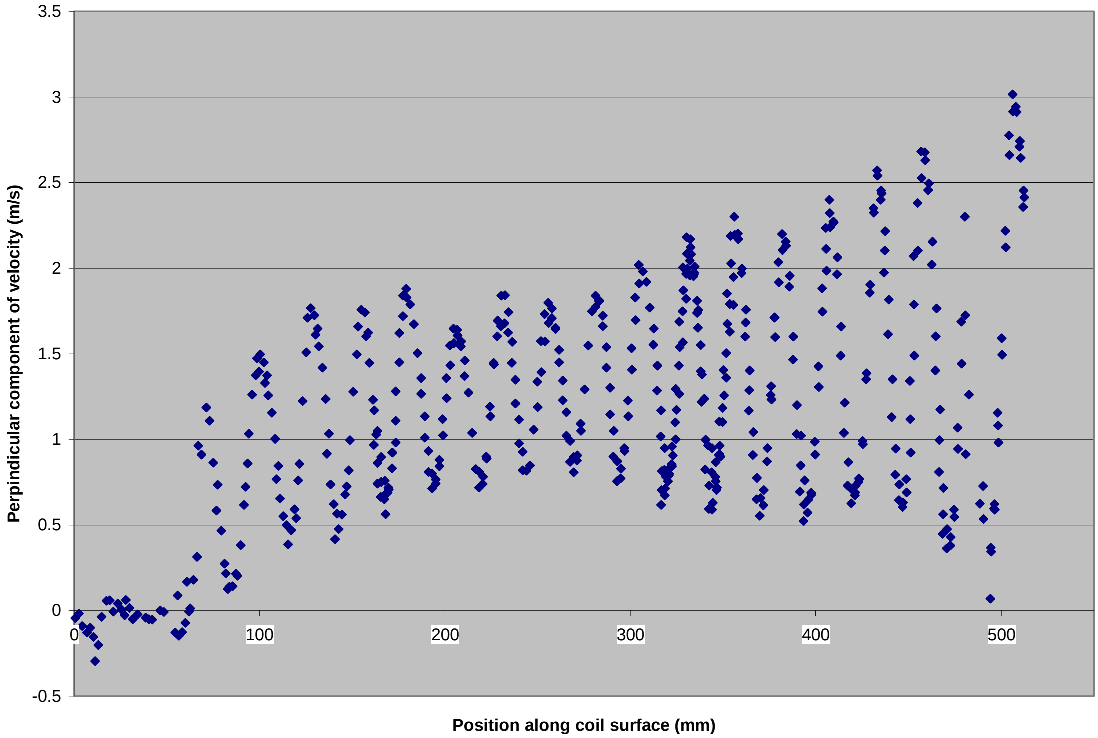

Figure 3.3 Velocity profile for exit from upper slab, dry coil at 1200 CFM, Test 1c

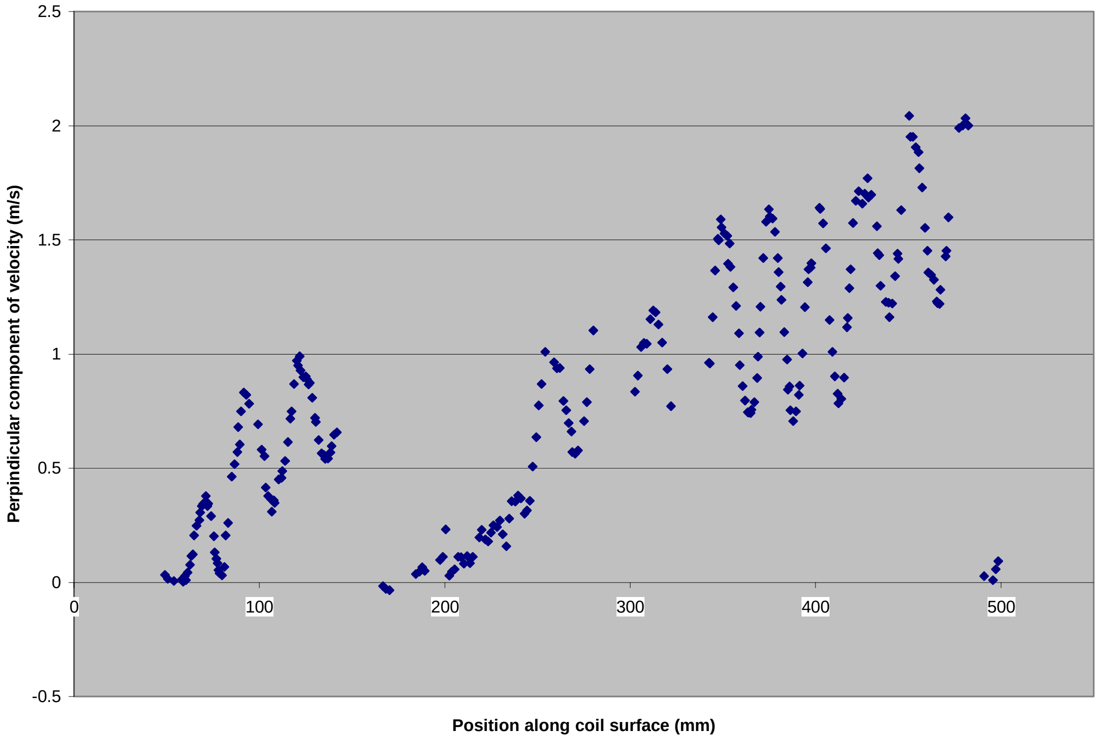

Figure 3.4 Velocity profile for exit from lower slab, dry coil at 1200 CFM, Test 1d

A plausible explanation for the distinct patterns seen in the different portions of the coil is that they are induced by the geometry of the coil and the features attached to it. Figure 3.5 is a sketch of the test coil showing three streamlines. In general, the fins impose a lot of flow resistance to the air relative to the other features in the duct. Therefore, the air's path of least resistance would be along a streamline that passes nearly perpendicularly through the coil. Since the flow has to turn into the coil at the inlet and into the duct at the coil exit, it would not be a perfectly straight path through the entire coil. The middle streamline in the figure represents the general flow path through the coil. Most of the middle section of the coil displays a somewhat constant velocity because the momentum resistance along these streamlines is not greatly affected by any of the neighboring regions.

The streamline near the top of Figure 3.5 shows a path affected by the mounting bracket. In this portion of the coil, the inlet closest to the base is obstructed and no air flow can enter here. Therefore, air flow must go around the bracket and enter the coil beyond this point. The portion of the coil inlet just beyond the mounting bracket must therefore be the entrance point for all of the air flowing along the path perpendicular through the coil as well as the entire region of the coil sealed off by the mounting bracket. This is the reason for the velocity spike just beyond the bracket at the coil inlet and the very low velocity near the base of the coil at the coil exit.

The bottom most streamline in Figure 3.5 depicts a path in the vicinity of the apex. Since a solid boundary is present at the apex of the coil, air in this region cannot follow the typical flow path because it cannot begin its turn into the duct before it exits the coil. For this reason, it must turn harder at the exit, which results in greater flow resistance, and therefore the flow is reduced in this region.

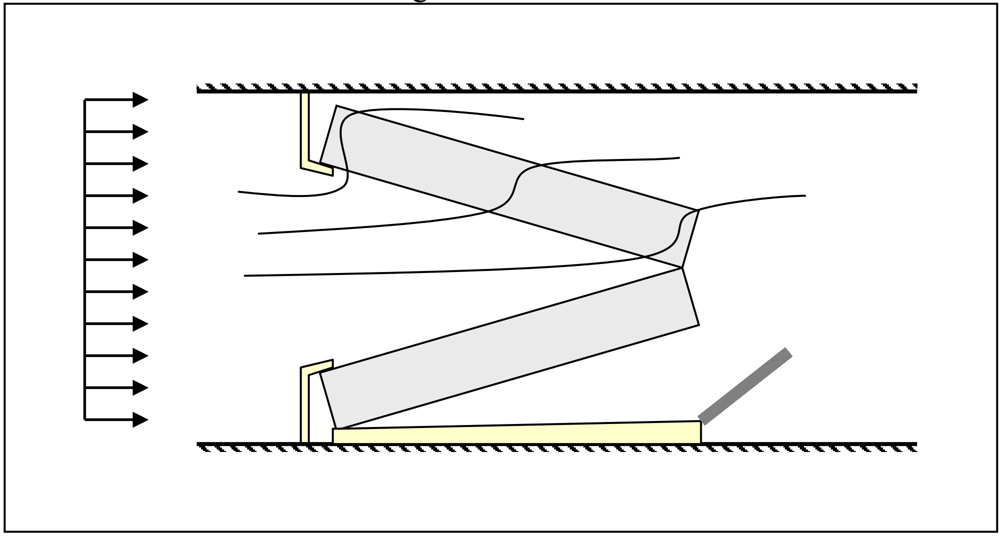

Figure 3.5 Air flow streamlines through A-shaped coil

3.2 Reduced Flow Tests (2a and 2b)

Inlet Velocity Measurements for 0.425 m^3s^{-1} (900 CFM) Dry Coil Tests

The next set of PIV measurements examined the dry coil case with a reduced air flow rate. For these tests, the target air flow rate was 0.425 m^3s^{-1} (900 CFM), which is 75 % of the manufacturer's suggested flow rate. We operated the test section with the target test conditions listed in the test matrix; the time averaged measured values throughout the duration of the tests are shown below and their uncertainty is calculated in Appendix A:

- Volumetric flow rate of air: 0.425 m^3s^{-1} (900.4 CFM)
- Air entering dry bulb temperature: 26.7 ºC (80.1 ºF)
- Air entering dew point temperature: 1.8 ºC (35.3 ºF), 20% RH
- Water inlet temperature: 7.1 ºC (44.7 ºF)
- Water mass flow rate: 284 gs^{-1} per slab

Throughout these tests the temperature increase of the water flowing through the heat exchanger was 3.7 ºC (6.7 ºF) for the upper slab and 3.1 ºC (5.6 ºF) for the lower slab. The total heat transfer at this flow rate was calculated to be 8.06 kW, of which 4.44 kW was transferred through the top slab and 3.63 kW was transferred through the bottom slab. Similar to the baseline test case, this again shows a difference of 22 %. Numerical integration of the PIV data showed that 18.1 % more air passed through the upper slab than the lower slab. The PIV measurements for the approach air flow to the upper and lower slabs of this coil are shown in Figure 3.6, the measurement uncertainty for these data sets ranged between 2.1 % and 3.3 % at 95 % confidence. This figure shows similar trends to the baseline test case (Figure 3.1), but with reduced velocity magnitudes.

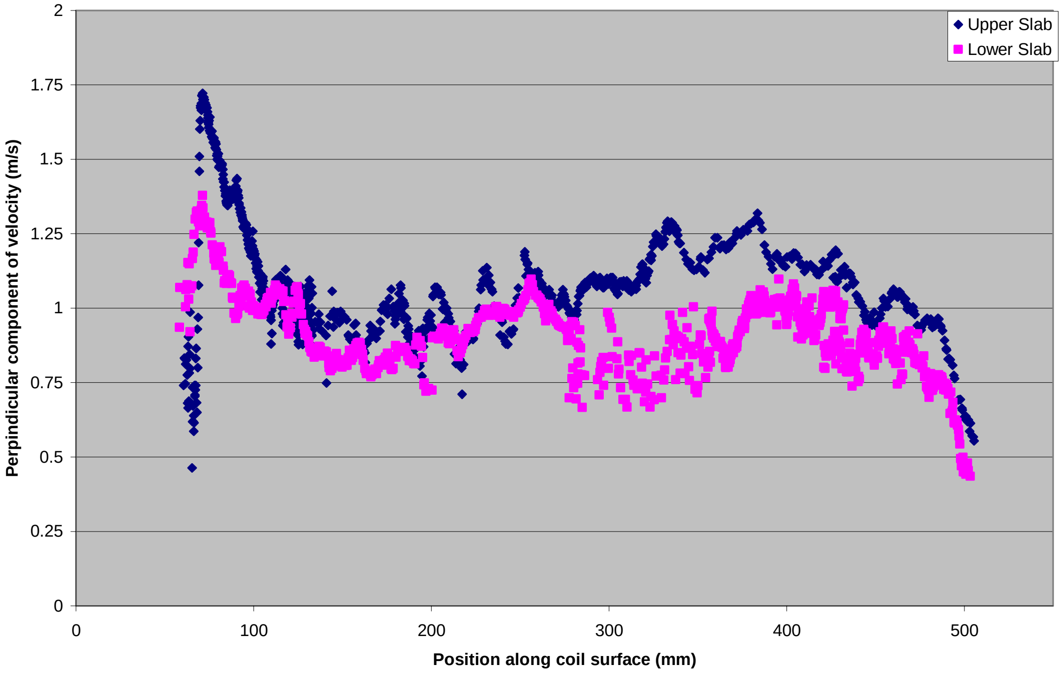

Figure 3.6 Velocity profiles for inlet to dry coil at 900 CFM, Tests 2a and 2b

3.3 Wet Coil Tests (3a, and 3b)

Inlet Velocity Measurements for 0.566 m^3s^{-1} (1200 CFM) Wet Coil Tests

For these tests, the target air flow rate was 0.566 m^3s^{-1} (1200 CFM) with a dry bulb temperature of 26.7ºC (80 ºF) and 50% humidity. The time averaged measured values throughout the duration of the tests are shown below.

- Volumetric flow rate of air: 0.568 m^3s^{-1} (1204 CFM)
- Air entering dry bulb temperature: 26.7 ºC (80.0 ºF)
- Air entering dew point temperature: 15.9 ºC (60.6 ºF), 52% RH
- Water inlet temperature: 7.4 ºC (45.3 ºF)
- Water mass flow rate: 286 gs^{-1} per slab

Throughout these tests the temperature increase of the water flowing through the heat exchanger was 5.9 ºC (10.6 ºF) for the upper slab and 5.2 ºC (9.4 ºF) for the lower slab. The total heat transfer at this flow rate was calculated to be 13.27 kW, of which 7.04 kW was transferred through the top slab and 6.23 kW was transferred through the bottom slab. Again, these measurements show that more heat is transferred through the top slab than the bottom; however, the difference in performance between these two slabs is not as great as with the dry coil tests. This set of data showed that the difference was approximately 13 %. Numerical integration of the PIV data showed that 33.1 % more air passed through the upper slab than the lower slab.

When the coil temperature is maintained below the dew point temperature of the air, water will condense out of the air as the air is cooled. The presence of the condensate in the finned tube coil creates a different flow situation from the dry coil case. From the air's perspective, the main issue is that the water takes up some of the volume inside the coil that would be available for the air to flow through. Therefore, flow through the coil is more resistive when the coil is wet. Figure 3.7 shows a picture of the test coil operating in a high humidity test.

There are a few reasons why the difference in heat transfer rate during the wet coil test is smaller than that during dry coil tests. First, we expect that the lower slab will have a higher latent capacity per unit air flow than the upper slab. This is because the air velocity is slower for the lower slab, which allows more time for water to condense on the surfaces of this coil. The second reason is that when water is condensed on the upper slab of the coil, it runs off onto the lower slab, and most of the condensation leaving the test coil drips out from the base of the lower slab. Because of the path that the water takes while it moves downward towards the base of the lower slab, the water is continuously being cooled until it leaves the coil. This means that some of the heat absorbed by the lower slab was used to subcool the condensate.

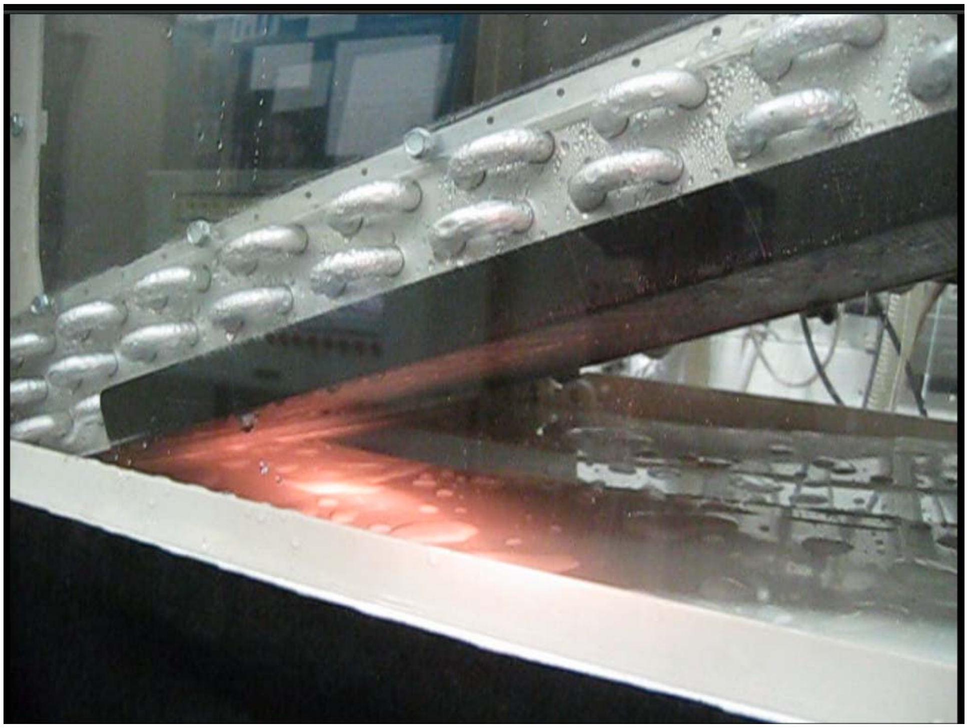

Figure 3.7 Test coil operating in wet coil test

Figure 3.8 shows the approach velocity profile for the upper and lower slab of the coil at the rated air flow rate with a dry bulb temperature of 26.7 ºC (80.0 ºF) and a dew point temperature of 15.9 ºC (60.6 ºF). In general, the data shows similar characteristics to the baseline test case. One difference is that the center region of each slab is flatter than the baseline test case, which means that the air flow seems to be more uniformly distributed across each slab. This is because the flow resistance is much greater in the wet coil since the water in the coil restricts the air's path through the coil; a more resistive slab will tend to keep the air flow more uniformly distributed. Another difference is that the lower slab does not display the very large spike in the entrance velocity near the base, as was seen in the other test cases. This is likely due the fact that there will be more water held in the lower slab since the flow path of the condensation runoff passes through it. Furthermore, the bottom of the lower slab will realize the highest concentration of water and therefore block more air flow through it. One last point is that the water runoff is continuously be cooled as it flows along the surface of the coil towards the drain; therefore, its viscosity will increase along its path which will be another factor that increases the air flow resistance near the bottom of the slab.

It is also important to note that there are a number of locations that show a much lower velocity than the neighboring locations. This is due to the fact that a water droplet on the coil surface would cause a temporary blockage and the measurement technique records velocity information based on instantaneous snapshots. Therefore, these low/no flow segments are not representative of the steady-state air velocity profile. Since water runoff is inherently a time dependent phenomenon, a better representation of the steady state velocity distribution could only be acquired by averaging multiple scans acquired with very large time between each. In general, though, the velocity distribution pattern is well represented in this figure.

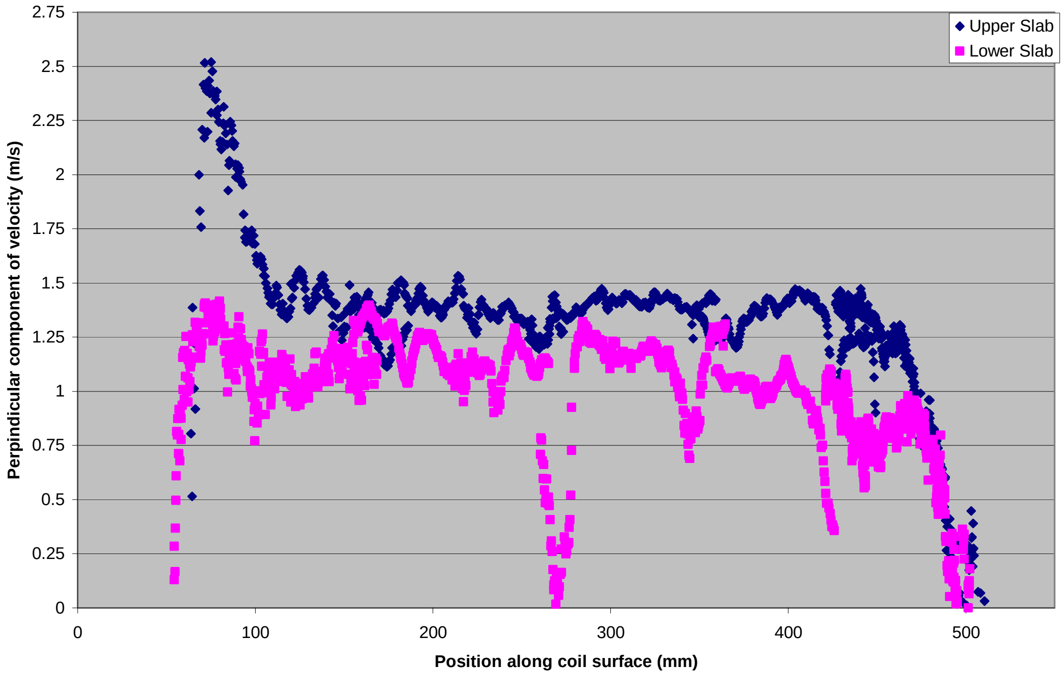

Figure 3.8 Velocity profiles for inlet to wet coil at 1200 CFM, Tests 3a and 3b

3.4 Wet Coil Reduced Flow Tests (4a, and 4b)

Inlet Velocity Measurements for 0.425 m^3s^{-1} *(900 CFM) Wet Coil Tests*

In the last set of PIV measurements, we measured the velocity profile under conditions of reduced air flow and moisture removal. The time averaged measured values throughout the duration of the tests are shown below.

- Volumetric flow rate of air: 0.422 m^3s^{-1} (894 CFM)
- Air entering dry bulb temperature: 26.7 ºC (80.1 ºF)
- Air entering dew point temperature: 15.7 ºC (60.2 ºF), 51 % RH
- Water inlet temperature: 7.4 ºC (45.2 ºF)
- Water mass flow rate: 285 gs^{-1} per slab

In line with the other measurements, this test case also showed that the upper slab of the heat exchanger transferred significantly more heat than the lower slab. In these measurements the temperature increase of the water flowing through the heat exchanger was 5.1 ºC (9.2 ºF) for the upper slab and 4.6 ºC (8.3 ºF) for the lower slab. The total heat transfer at this flow rate was calculated to be 11.58 kW, of which 6.12 kW was transferred through the top slab and 5.46 kW was transferred through the bottom slab; a difference of approximately 12 %. Numerical integration of the PIV data showed that 15.2 % more air passed through the upper slab than the lower slab. Figure 3.9 shows the measured velocity profiles approaching the test coil.

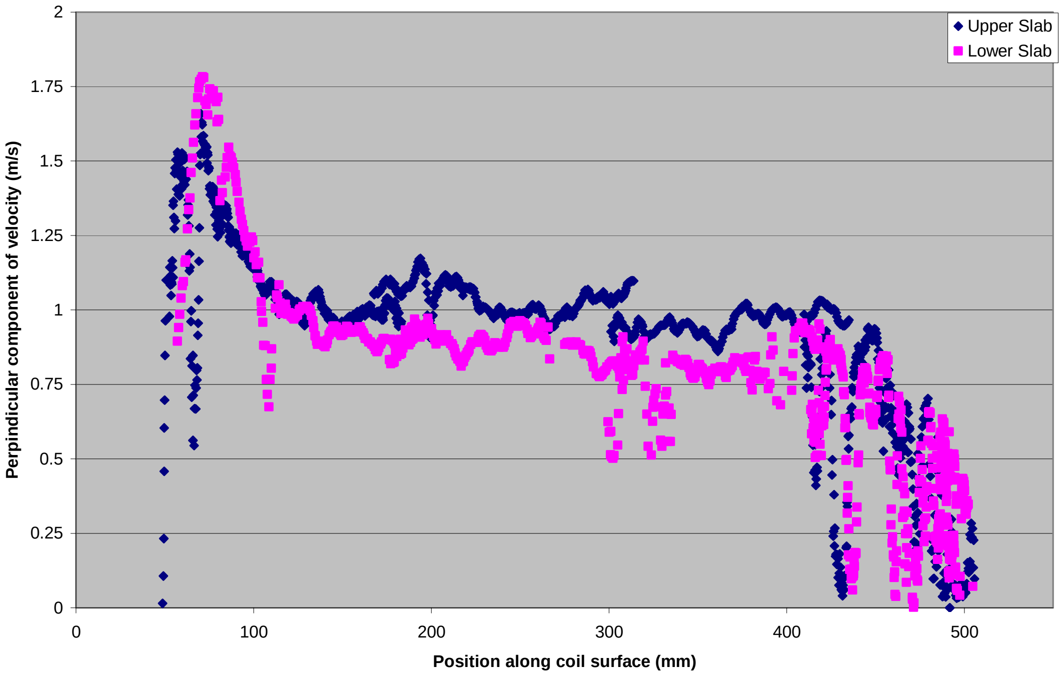

Figure 3.9 Velocity profiles for inlet to wet coil at 900 CFM, Tests 4a and 4b

The data from these measurements again show that the condensation tends to smooth out the velocity profile in the middle portion of the slabs. It is interesting, however, that this test case shows the presence of the velocity spike region on the surface of the lower coil, which was not present in the 0.566 m^3s^{-1} (1200 CFM) wet coil test case. A possible explanation is that the rate of moisture removal from the 0.425 m^3s^{-1} (900 CFM) wet coil test case is lower than during the 0.566 m^3s^{-1} (1200 CFM) wet coil test case, and this lower rate of condensation runoff does not produce enough water to result in the additional resistance needed to alter the air velocity profile in the lower portion of the lower slab as in the 0.566 m^3s^{-1} (1200 CFM) wet test case.

4. CFD SIMULATIONS

Our CFD-based model of the heat exchanger was constructed through a momentum resistance modeling approach. Momentum resistance models are used to model flow domains that include obstructions or elements which are smaller than the desired grid resolution. This method is based on the idea that we can model the momentum resistance imparted to the flow by these elements by characterizing the pressure drop using lumped parameters, called momentum resistance coefficients, and assigning them to nodes that reside within the resistive domain.

4.1 Model

The starting point for our simulations was the preparation of a 2-dimensional geometrical representation of the test coil and the attached ducting. The computational domain is shown below in Figure 4.1; the flow in this case is left to right.

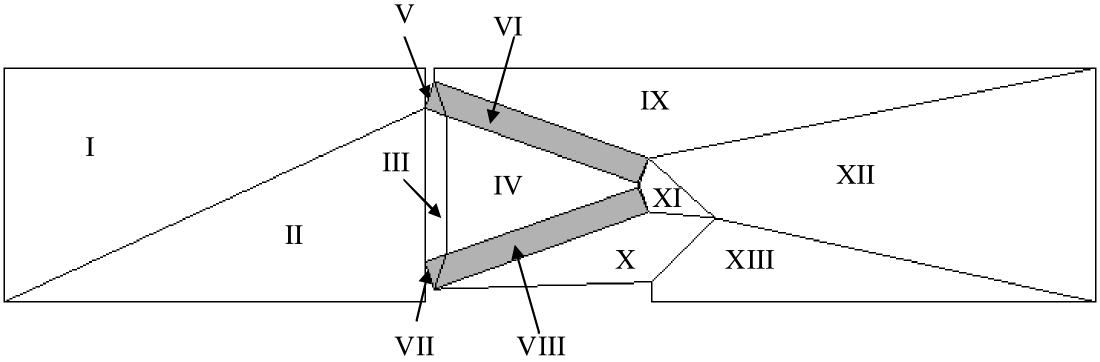

Figure 4.1 Computational domain for CFD analysis

In the figure above, the entire computational domain is divided into 13 sub-domains, each being a four sided structure (some sides were divided into two sections in order to make all sub-domains four sided). Sub-domains I and II represent the flow field in the duct upstream of the test coil. Sub-domain III represents the region at the inlet to the base of the heat exchanger where entrance to the coils are blocked by the mounting bracket; the borders between this sub-domain and the heat exchanger slabs are modeled as thin walls, i.e., fixed boundaries which flow cannot pass through. Sub-domain IV represents the area in between the upper and lower slabs of the heat exchanger. Sub-domains V and VI represent the upper slab and sub-domains VII and VIII represent the lower slab; each slab was broken into two subdomains in order to model the solid boundary from the mounting bracket. Sub-domains IX and X represent the regions at the exit of the upper and lower slabs, respectively. The condensation collection pan is modeled by the lower boundary of sub-domain X and the metallic insert to the collection pan is modeled by the thin wall boundary between sub-domain X and XIII. The right hand side of sub-domain XII represents the test section exit. The coordinates used to model this geometrical set are listed in Appendix B.

Each line in the above figure was divided by 15 nodes. We spaced the nodes using a single-sided geometric transition factor of 1.2 for the entities within sub-domains I, II, IX, XII, and XIII; and a double sided geometric transition factor of 1.2 for entities in all other sub-domains. We then set boundary conditions along each entity in Figure 4.1. We set the inlet boundary (far left side of sub-domain I) with fixed velocity and pressure conditions. We set the exit boundary (far right side of sub-domain XII) using fixed farfield velocity and pressure conditions. The entities representing the portions of the mounting bracket that obstructed the coil inlet at the base and the metallic condensation catch tray were modeled as thin walls; therefore we assigned values of zero velocity to each node along these entities. All of the entities along the top and bottom of the computational domain were representative of the duct walls and were treated as solid boundaries; the entities located at the test section apex were also treated as solid boundaries. All other entities were treated as general interfaces between sub-domains and were therefore unbounded.

4.2 Baseline Test Case: 0.566 m^3s^{-1} (1200 CFM) Dry Coil, Test 1

We performed the first set of simulations to replicate the baseline test case of 0.566 m^3s^{-1} (1200 CFM) air flow rate without moisture removal. Prior to beginning the simulations, we performed necessary calculations to determine certain input parameters. All thermophysical properties of air were calculated using Refprop 8.0 (Lemmon et al., 2007).

The first step was to determine the coefficients to model the heat exchanger as momentum resistance sub-domains. In the momentum resistance model, the pressure gradient is related to the velocity through the following relationship:

$$\nabla P = \rho\left(\frac{\lfloor K_l \rfloor}{2\beta} + \left|\vec{V}\right| \frac{\lfloor K_q \rfloor}{2\beta^2}\right) \cdot \vec{V}$$

where P is the pressure, ρ is the air density, K_l and K_q are linear and quadratic momentum resistance coefficient matricies, β is the porosity factor (flow volume/total volume), and $\vec{V}$ is the velocity. This momentum resistance term is then included in the momentum conservation equation in the CFD solver. In order to determine these coefficients, we used laboratory data of air side pressure drop through the coil at various flow rates.

We measured the pressure difference across the lower slab of the coil using a differential pressure sensor calibrated to within 0.7 Pa (0.003" H_20) over the range of 12 Pa to 40 Pa (0.05" H_2O to 0.16" H_2O), with the taps located upstream and downstream of the lower slab as shown in Figure 4.2. We measured the air-side pressure difference at six different air flow rates; this pressure drop data is shown in Appendix C. When we examined the results of the PIV measurements, we saw that approximately 45 % of the air flows through the lower slab and 55 % of the air flows through the upper slab; therefore, we multiplied the measured flow rate by 0.45 to correlate against the measured pressure drop through the lower slab.

Figure 4.2 Static pressure taps used to measure air side pressure drop through lower slab

We made a simplifying assumption that the pressure drop measured during this data collection was realized linearly through the coil; therefore, we approximated the pressure gradient by dividing the pressure difference by the thickness of the lower slab. We then calculated the average velocity as the volumetric air flow through the lower slab divided by the face area of the slab. We then fit a curve to the measured data using a least squares regression and the following functional form:

$$\frac{\partial P}{\partial x} = C_l\left[u\right] + C_q\left[u\right]^2$$

The values of the coefficients C_q and C_l were determined to be:

$$C_q = 239.4\,\frac{\text{kg}}{\text{m}^4}$$

$$C_l = 15.96\,\frac{\text{kg}}{\text{s}\cdot\text{m}^3}$$

$$R^2 = 0.986$$

C_q and C_l were then used to calculate the momentum resistance coefficients K_q and K_l through the following relationships:

$$K_l = \frac{2C_l}{\rho} = \frac{2\cdot\left(15.96\,\frac{\text{kg}}{\text{s}\cdot\text{m}^3}\right)}{1.184\,\frac{\text{kg}}{\text{m}^3}} = 27.0\,\frac{1}{\text{s}}$$

$$K_q = \frac{2C_q}{\rho} = \frac{2\cdot\left(239.4\,\frac{\mathrm{kg}}{\mathrm{m}^4}\right)}{1.184\,\frac{\mathrm{kg}}{\mathrm{m}^3}} = 404.4\,\frac{1}{\mathrm{m}}$$

These values of K_q and K_l were used to characterize the momentum resistance inside the heat exchanger sub-domains under dry conditions.

The other parameters necessary to begin the simulations were the inlet and exit velocity for the boundary conditions. In the baseline test case, we divided the total flow rate by the total height of the duct and the lateral width of the heat exchanger inlet. We used the lateral width of the coil inlet rather than the lateral width of the duct since we constructed a 2-dimensional model and this approach accounts for all of the air flow through the coil. In this case, we found the average velocity for the inlet and exit farfield conditions as:

$$\bar{V} = \frac{\left(0.5663\,\frac{\mathrm{m}^3}{s}\right)}{(0.5207\ \mathrm{m})\cdot(0.4572\ \mathrm{m})} = 2.3789\,\frac{\mathrm{m}}{\mathrm{s}}$$

We used these terms as input for the baseline test case to simulate the air flow through the test section and converged upon the solution shown in Figure 4.3. Here we can see how the air flows around the abrupt step into the coil entrance, from sub-domains I and II into sub-domain III, then nearly perpendicular through the heat exchanger coils, and finally into the discharge sections.

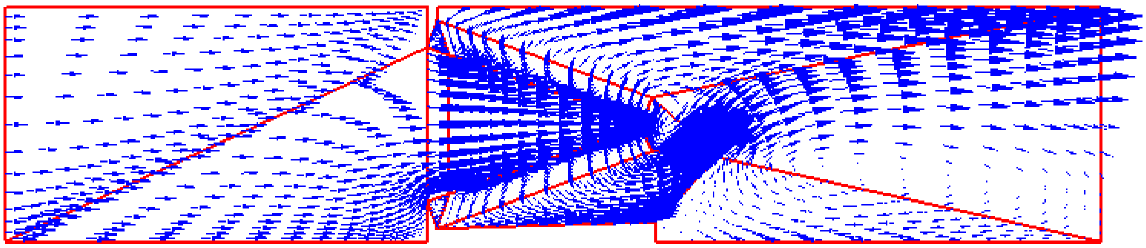

Figure 4.3 Vector field representation of CFD results for flow through dry coil at 1200 CFM

Some useful information from these simulations is clearly identified in Figure 4.4, which plots the stream function through the computational domain. First, close inspection of the entrance to the heat exchangers shows that the areas near the base are somewhat starved for air flow because of the mounting brackets. Also, note that the flow leaving the lower slab must rapidly turn upwards because of the condensation tray, which causes the path through the lower slab to be much more resistive than the path through the upper slab; therefore more streamlines pass through the upper slab. One last item of interest is the large recirculation zone downstream of the condensation tray; this zone was clearly visible during the laboratory PIV measurements due to the fog entrained in the flow.

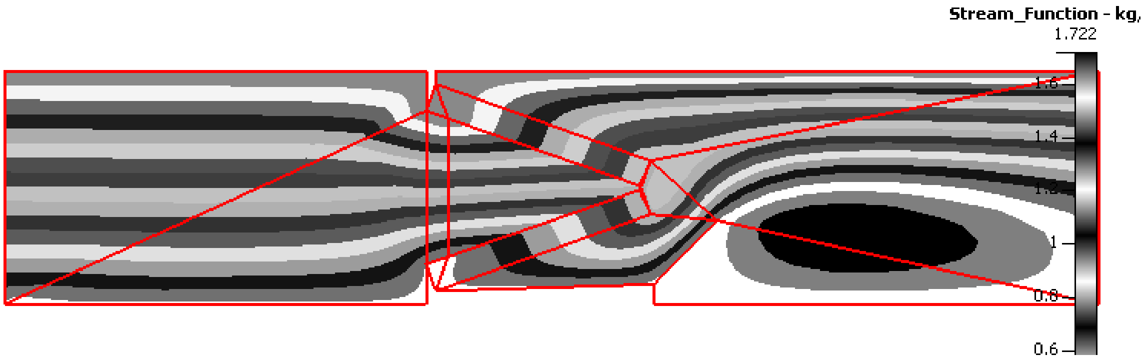

Figure 4.4 Streamlines for flow through dry coil at 1200 CFM

Figure 4.5 compares the results of the simulation at the entrance to the upper slab of the test coil with the PIV measurements taken at the same location. In this figure, all data is plotted as the perpendicular component of velocity versus the position along the coil surface. The CFD data is shown for five different positions upstream: right at the coil surface, and at 1 mm, 5 mm, 10 mm, and 15 mm upstream of the coil surface; the PIV data was collected at locations ranging from 5 to 16 mm upstream of the coil surface. The contours are all slightly different indicating that the air flow redistributes itself as it approaches the coil.

Overall, the CFD results fit the measured data very well. Over 93 % of the span of the coil, the simulated values at 10 mm upstream fit the measured data within ±15 %. The CFD data shows the same features as the PIV data, namely the velocity peak after the mounting bracket and the declining velocity near the apex.

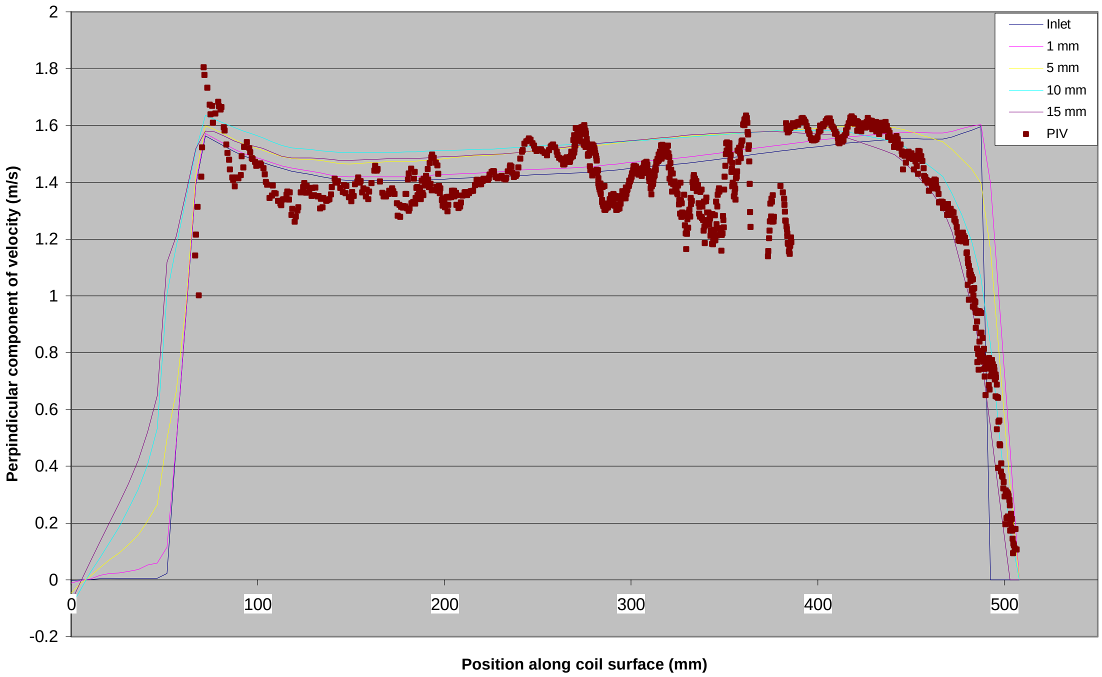

Figure 4.5 PIV and CFD data for inlet to upper slab at 1200 CFM dry coil, Test 1a

Figure 4.6 shows the PIV and CFD results for the inlet to the lower slab under dry coil conditions and 1200 CFM air flow rate. Again, the results for the CFD simulations are shown at the inlet, 1 mm, 5 mm, 10 mm, and 15 mm upstream of the coil surface, while the PIV data was taken within the range of 6 mm to 14 mm upstream of the coil surface. The PIV data shows a larger velocity peak, whereas the CFD data shows the velocity peak near the base to be more in line with the data from the upper slab. Another difference is that the CFD data shows a second velocity peak approximately 50 mm from the apex, whereas the PIV data does not show this. Both of these sections are within regions where very large velocity gradients are present along their streamlines. In the 60 mm to 100 mm region, the magnitude of the velocity spike is under-predicted by the simulation because it is difficult to resolve the large velocity gradients in this region. The simulation also shows a second peak near the apex; this is because the velocity gradients just downstream of the heat exchanger slab in this region are extraordinarily large (see Figure 4.3) and also difficult to resolve. Overall, the agreement is not as good as for the upper slab, but can be considered as adequate. Over 82 % of the span of the coil the simulated values at 10 mm upstream fit the measured data within ±20 %.

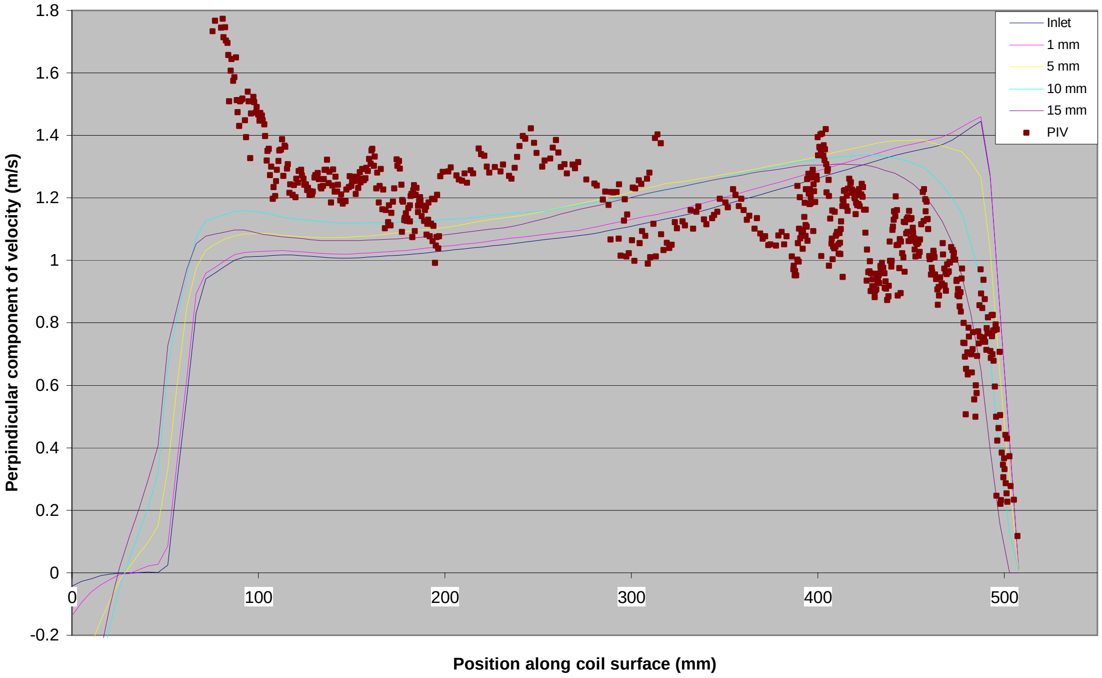

Figure 4.6 PIV and CFD data for inlet to lower slab at 1200 CFM dry coil, Test 1b

Figure 4.7 shows the data for the exit side of the upper slab. This figure shows the CFD data right at the exit of the heat exchanger, as opposed to various distances downstream, because the simulated exit velocity profiles did not change with distance from the slab. As discussed in the previous section, the PIV data shows a very large sinusoidal component to the velocity profile. This sinusoidal component exists because the air is directed out of the heat exchanger through the gaps between adjacent tubes in the last depth row. The sinusoidal component is not seen in the CFD solution because the heat exchanger slabs were modeled as homogeneous resistive domains.

Overall, both the PIV and CFD data sets show the same general trend. The lowest positions correspond to those where the exit from the slab is closest to the duct, and in this pinched corner the flow is slower than the rest of the coil. The velocity rapidly increases with position for the initial portion of the coil, then mildly increases along the remainder of the coil, until it drops to zero at the apex. It is difficult to compare the fitness of the simulation values with the measured data because the simulation does not display the sinusoidal component seen in the measured data. However, the steady component of velocity may be a more useful tool to estimate the flow distribution, and the simulated data appears to lie directly in the vicinity of this component.

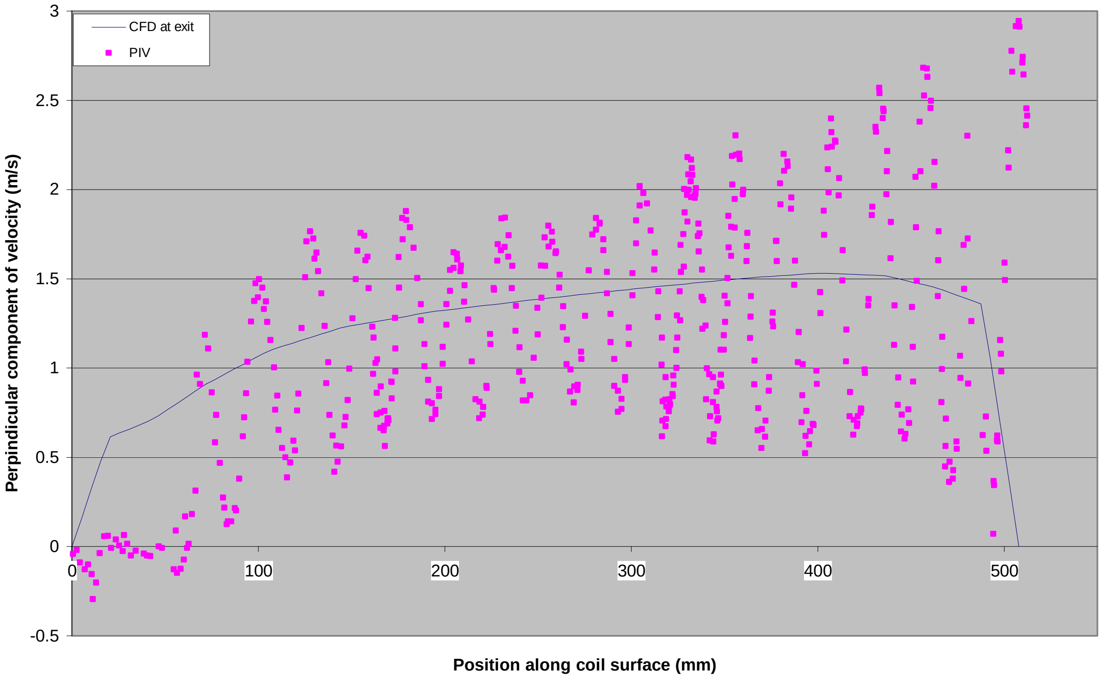

Figure 4.7 PIV and CFD data for exit from upper slab at 1200 CFM dry coil, Test 1c

Figure 4.8 shows the data for the flow exiting the lower slab of the test coil. This figure shows similar results to that of Figure 4.7, but the velocity in the corner at the base of the coil is much lower because the condensation pan occupies a considerable volume in this region. The condensation pan also forces more air flow towards the apex, resulting in a very well pronounced velocity spike. Again, the CFD solution offers a good representation of the average velocity profile without the sinusoidal component.

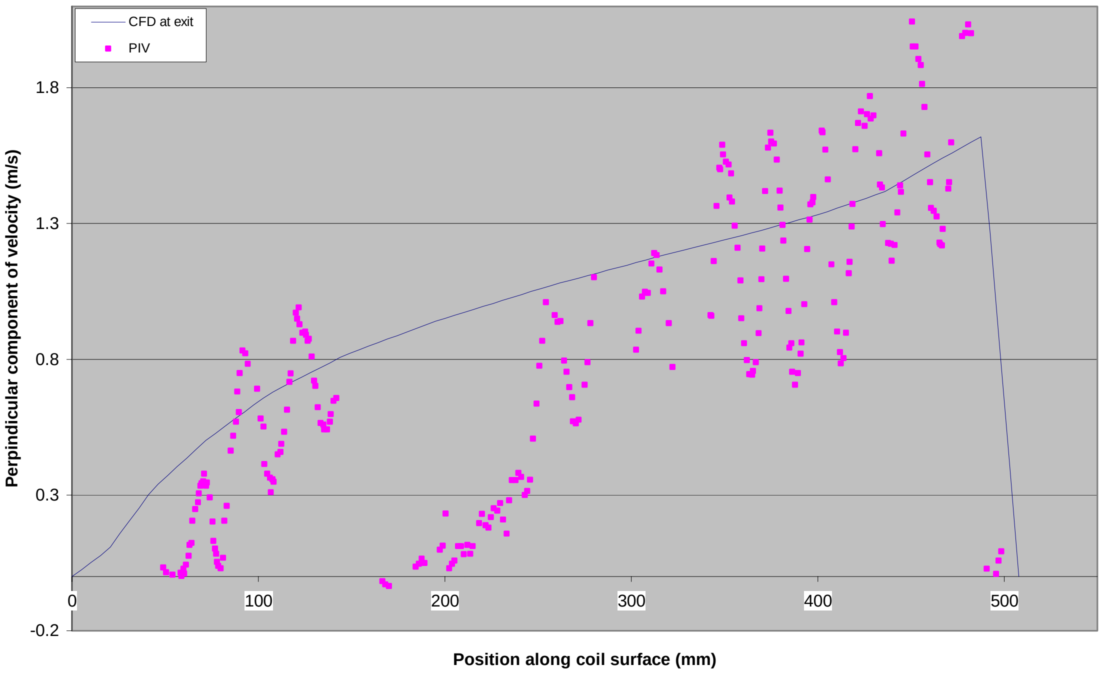

Figure 4.8 PIV and CFD data for exit from lower slab at 1200 CFM dry coil, Test 1d

By comparing the data in Figures 4.5, 4.6, 4.7, and 4.8 we notice that the velocity profiles for a given slab change between the inlet and the outlet. This indicates that the air does not flow through each slab in a strictly perpendicular path, and that there is some rearrangement of the air flow within the heat exchanger. This is logical because certain regions, such as the base end blocked off by the mounting bracket, receive no air at the inlet but must match the pressure at the exit.

Since the simulation results of the inlet and outlet of both heat exchanger slabs agree fairly well with the measured data, we can assume that the CFD solution of the air flow inside the coil is reasonably accurate. This information is very interesting because it is a key factor for determining the air-side heat transfer coefficients. Figure 4.9 shows a map of the velocity magnitude (combined parallel and perpendicular components) overlaid with an array of circles representing the placement of tubes in the heat exchanger. This figure shows that there are 8 tubes in the lower slab and 4 tubes in the upper slab that are exposed to air velocities below 0.4 ms^{-1}. These tubes will significantly underperform from a heat transfer point of view.

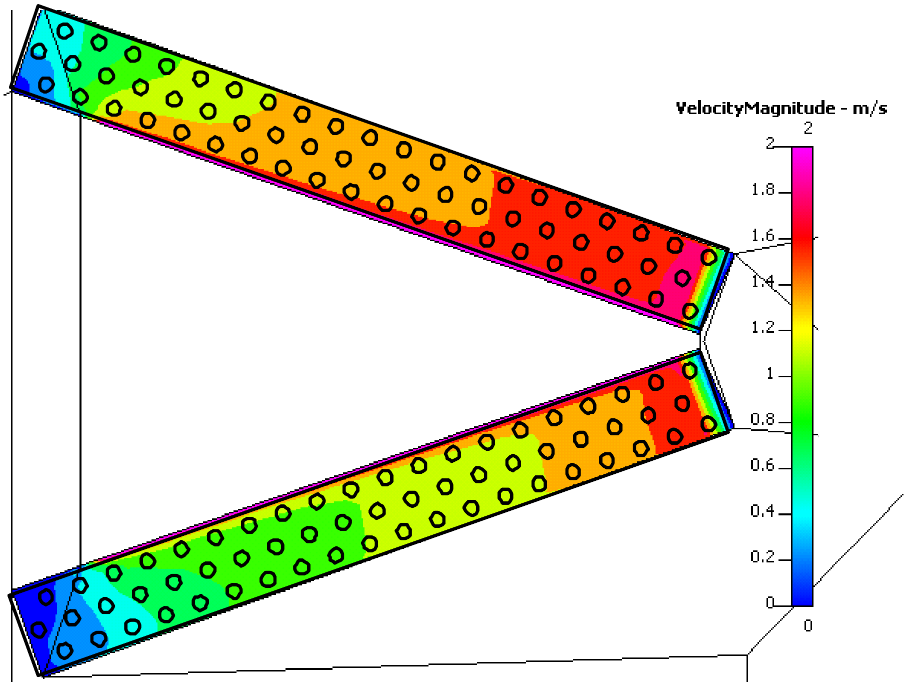

Figure 4.9 Map of velocity magnitude for 1200 CFM dry coil, Test 1

Figure 4.10 shows a close up of the streamlines passing through the upper slab of the heat exchanger. There are a few points of interest illustrated in this figure. First, examination of the top portion of the slab shows how the mounting bracket affects the flow. Air enters this section just beyond the mounting bracket and fans out to fill the uppermost region of the slab. This figure also illustrates how the streamlines turn near the entrance to pass perpendicularly through the coil.

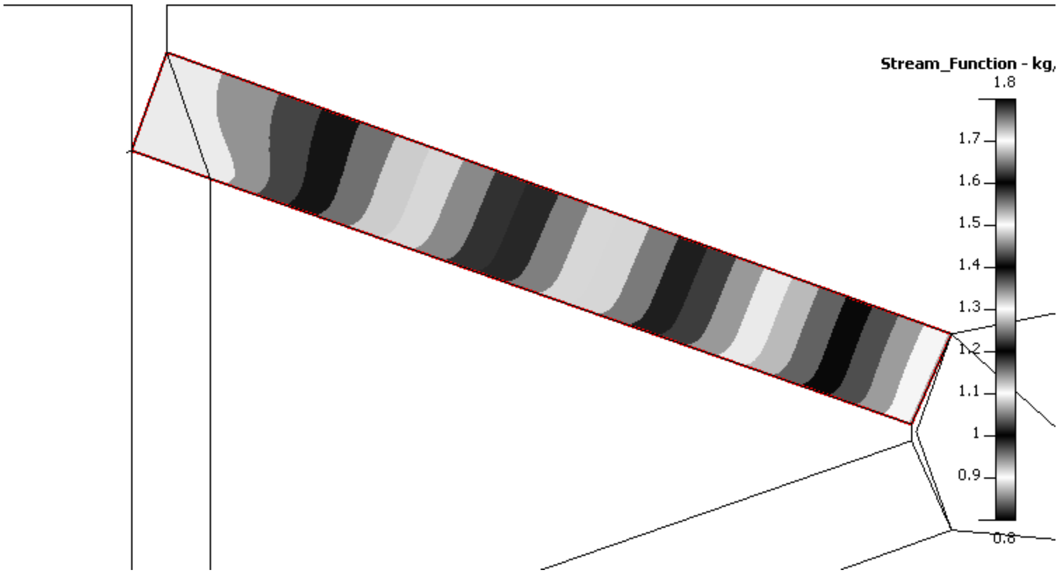

Figure 4.10 Close up of streamlines through upper slab of test coil, Test 1.

4.3 Reduced Air Flow Test Case: 0.425 m^{3}s^{-1} (900 CFM) Dry Coil, Test 2

The next set of simulations had the goal of predicting the air flow under dry coil conditions with a reduced air flow rate. In order to perform this set of simulations, we changed one input parameter, the average velocity for the inlet and exit farfield boundary conditions. The value for this input was 75 % of that used in the baseline test case.

$$\bar{V} = \frac{\left(0.4248\frac{\mathrm{m}^3}{s}\right)}{(0.5207\ \mathrm{m})\cdot(0.4572\ \mathrm{m})} = 1.7842\frac{\mathrm{m}}{\mathrm{s}}$$

We used this velocity, and the domain and parameters already in place, to simulate the low flow dry coil test case. The results of the inlet velocity profile for the upper and lower slabs are shown in Figures 4.11 and 4.12, respectively. The results are presented in the same manner as in the other figures. The PIV data was taken at upstream distances between 4 mm and 8 mm from the coil surface on the upper slab, and between 9 mm and 15 mm from the lower slab.

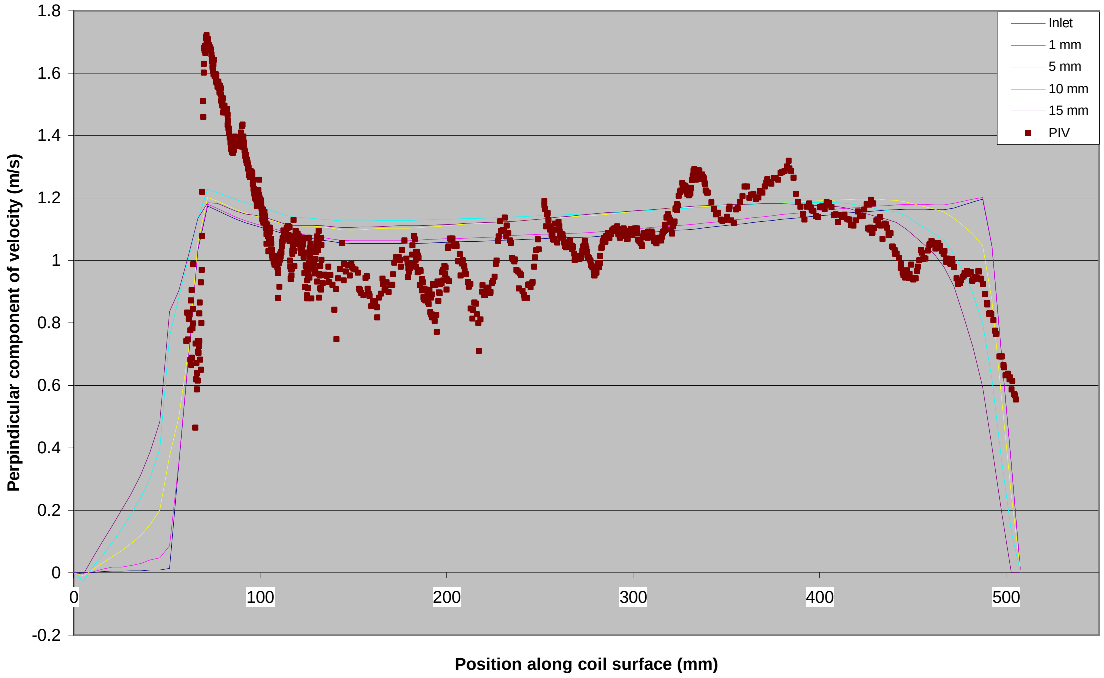

Figure 4.11 PIV and CFD data for inlet to upper slab at 900 CFM dry coil, Test 2a

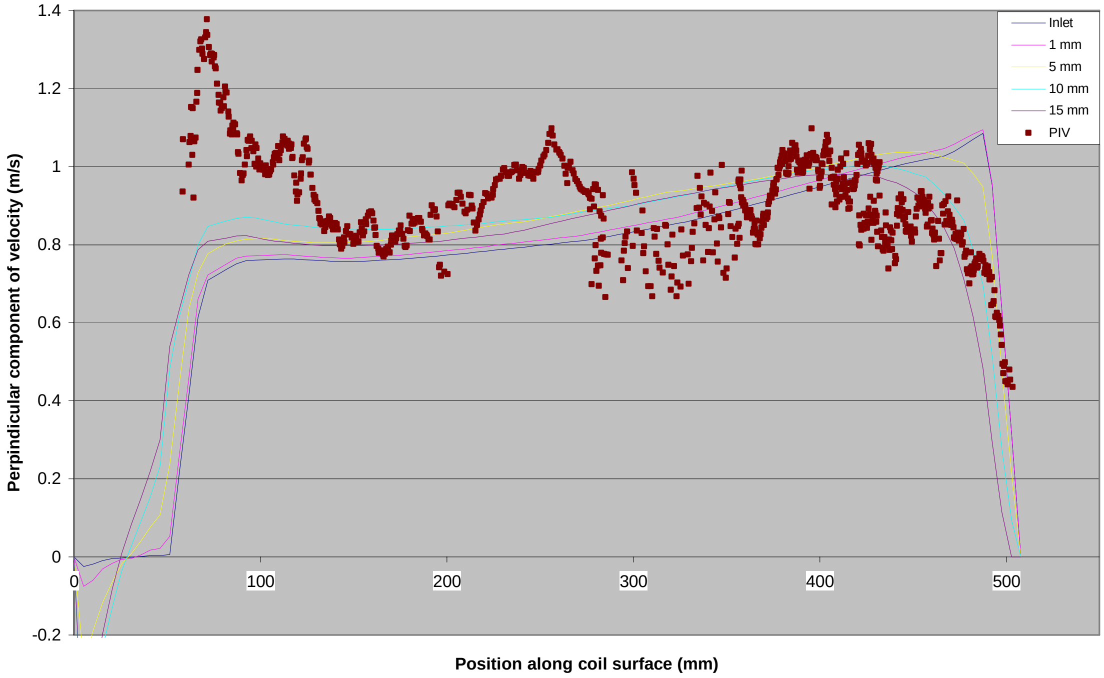

Figure 4.12 PIV and CFD data for inlet to lower slab at 900 CFM dry coil, Test 2b

The agreement between the simulated and measured data is similar to that obtained for 1200 CFM baseline test case. The CFD at 5 mm upstream and PIV data agree very well for the upper slab, with data over 78 % of the coil agreeing within ±15 %. The simulated velocity spike is not as large as the measured data on both slabs. For the lower slab, the 15 mm upstream CFD data matched the measured data within ±20 % over 86 % of the coil. The CFD model again predicted a region of increased velocity near the apex which is not shown by the PIV data.

Figure 4.13 shows the velocity magnitude map overlaid with the circles representing the placement of tubes in the heat exchanger for the 900 CFM dry coil test case. The general trends are similar to the baseline case, showing the same tube positions with low air flow.

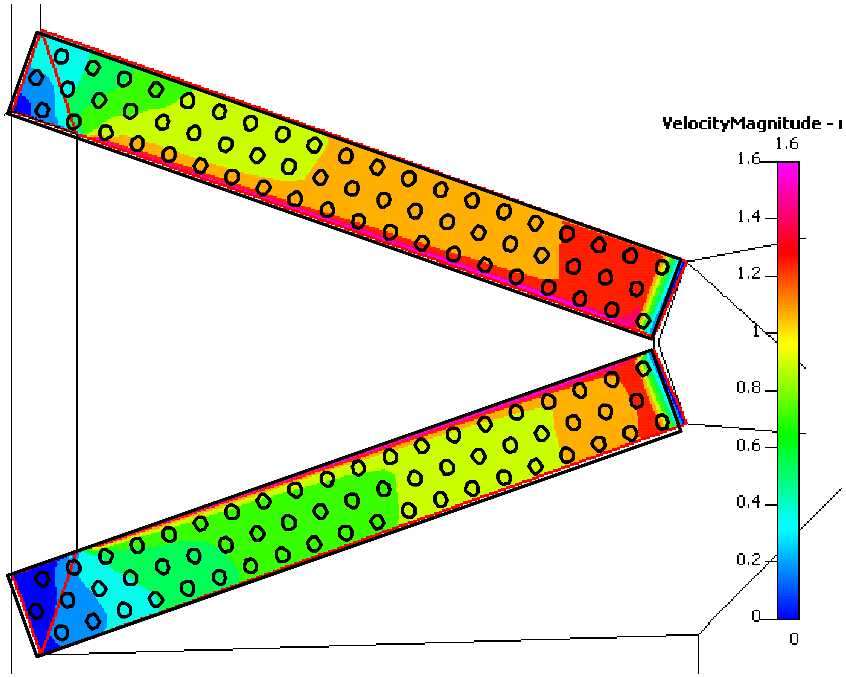

Figure 4.13 Map of velocity magnitude for 900 CFM dry coil, Test 2

4.4 Wet Coil Test Case: 0.566 m^{3}s^{-1} (1200 CFM), Test 3

We had to make some simplifications to perform simulations with a wet coil. In terms of momentum resistance, the wet coil situation differs from the dry coil because the water present between fins increase the flow resistance at that specific location. The water droplets are not stationary, and most of them roll down the coil until they are expelled from the base. This means that the momentum resistance of the slab is variable in time and space with a higher concentration of water near the bottom of the slab. Furthermore, the water content is strongly affected by the rate of moisture removal from the air, which is dictated by the air condition and the air flow rate.

Considering the complexity of assigning momentum resistance coefficients to the slabs of the test coil, we examined the measured pressure drop and flow rate for the wet coil laboratory experiments. The 1200 CFM test case maintained a pressure difference across the lower coil of 38.93 Pa, and the 900 CFM test case maintained a pressure difference across the lower coil of 30.94 Pa. We used the same analysis as performed in the previous section and determined that a quadratic curve that passes through these points and has a zero intercept is concave down; i.e., the quadratic coefficient is negative. This is not a physically feasible coefficient. This indicates that the flow situation with moisture removal is much more complicated than can be accurately described in this manner. However, we opted to use a linear regression with this data to find a single linear coefficient since the quadratic coefficient for this functional form is small relative to the linear coefficient. In this case we determined the value of C_l through a linear regression of:

$$\frac{\partial P}{\partial x} = C_l\left[u\right]$$

$$C_l = 597.21\frac{\text{kg}}{\text{s}\cdot\text{m}^3}$$

$$R^2 = 0.939$$

C_l was then used to calculate the linear momentum resistance coefficient K_l:

$$K_l = \frac{2C_l}{\rho} = \frac{2\cdot\left(597.21\frac{\text{kg}}{\text{s}\cdot\text{m}^3}\right)}{1.184\frac{\text{kg}}{\text{m}^3}} = 1008.8\frac{1}{\text{s}}$$

and assigned a value of zero to the quadratic momentum resistance coefficient, K_q.

Using these values for the momentum resistance coefficients and the boundary conditions for the baseline test case, we simulated the air flow field for the 1200 CFM wet coil test case. The results of the inlet velocity profile for the upper and lower slabs are shown in Figures 4.14 and 4.15, respectively. The results are presented in the same manner as in the other figures. The PIV data was taken at upstream distances between 5 mm and 19 mm from the coil surface on the upper slab, and between 11 mm and 18 mm on the lower slab.

It appears that the approach we used is generally acceptable but resulted in a local mismatch between the PIV and simulated values near the apex. The simulated data at 15 mm upstream matched the upper slab PIV data within ±15 % over 89 % of the coil, and the lower slab data within ±20 % over 84 % of the coil. The one area where there seems to be an obvious mismatch between the measured and simulated results is the secondary peak seen near the apex. This secondary peak is likely the result of the simplified linear representation of the momentum resistance coefficient, which underestimates the flow resistance of regions with locally high velocities.

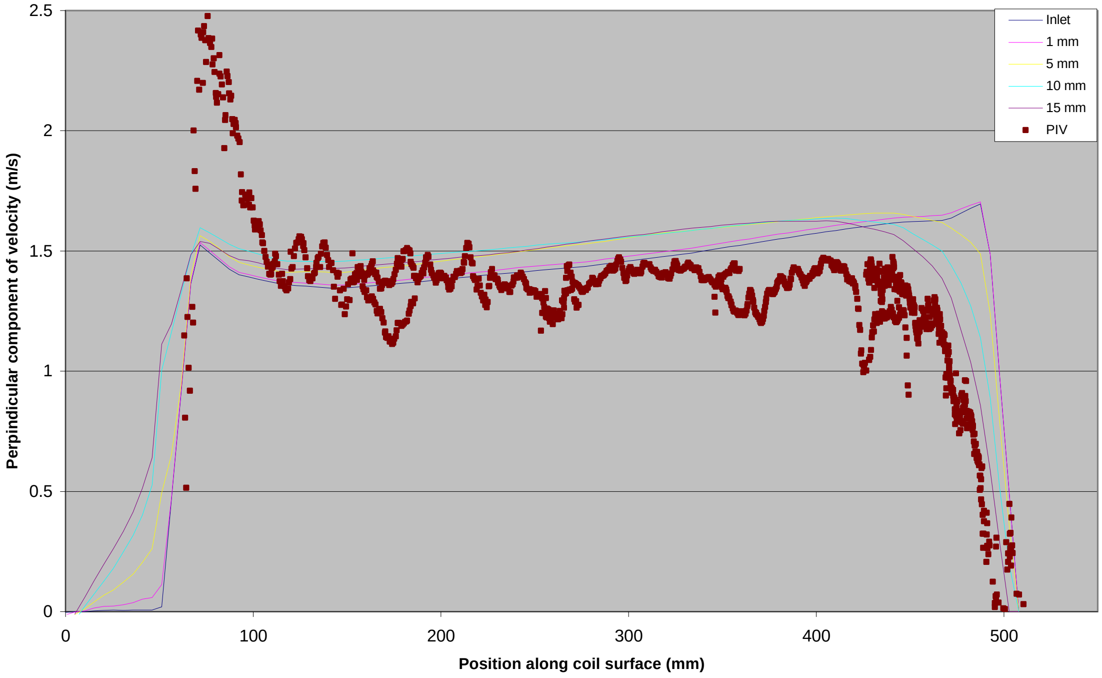

Figure 4.14 PIV and CFD data for inlet to upper slab at 1200 CFM wet coil, Test 3a

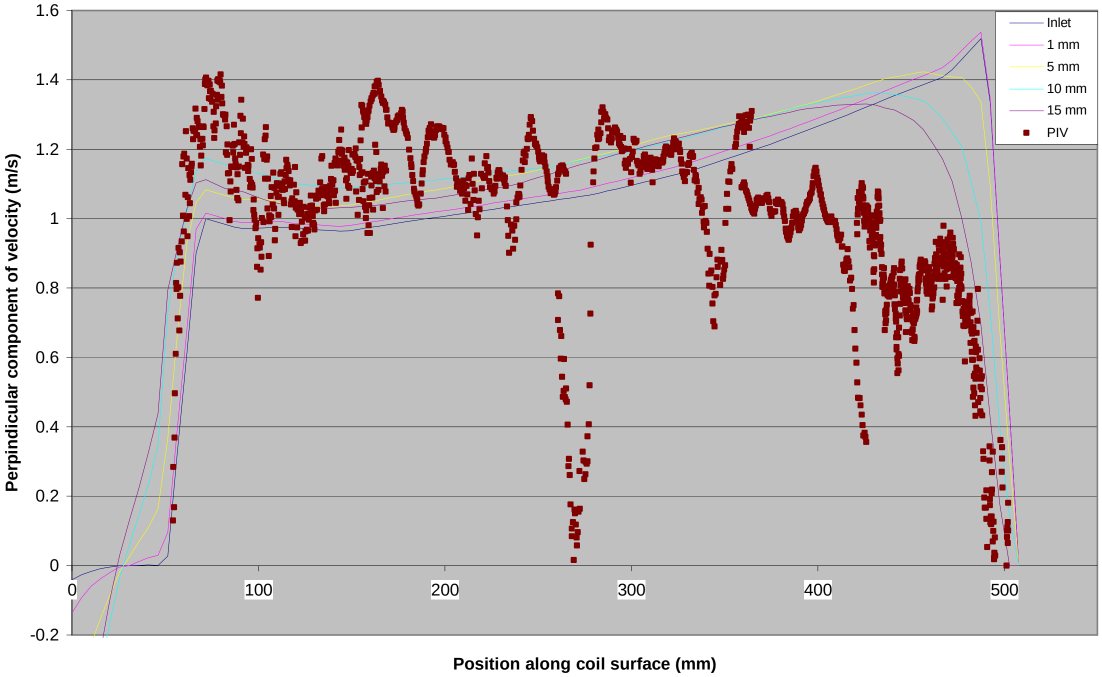

Figure 4.15 PIV and CFD data for inlet to lower slab at 1200 CFM wet coil, Test 3b

Figure 4.16 shows the velocity magnitude map overlaid with the circles representing the placement of tubes in the heat exchanger for the 1200 CFM wet coil test case. The general trends are similar to the baseline case, showing the same tube positions with low air flow.

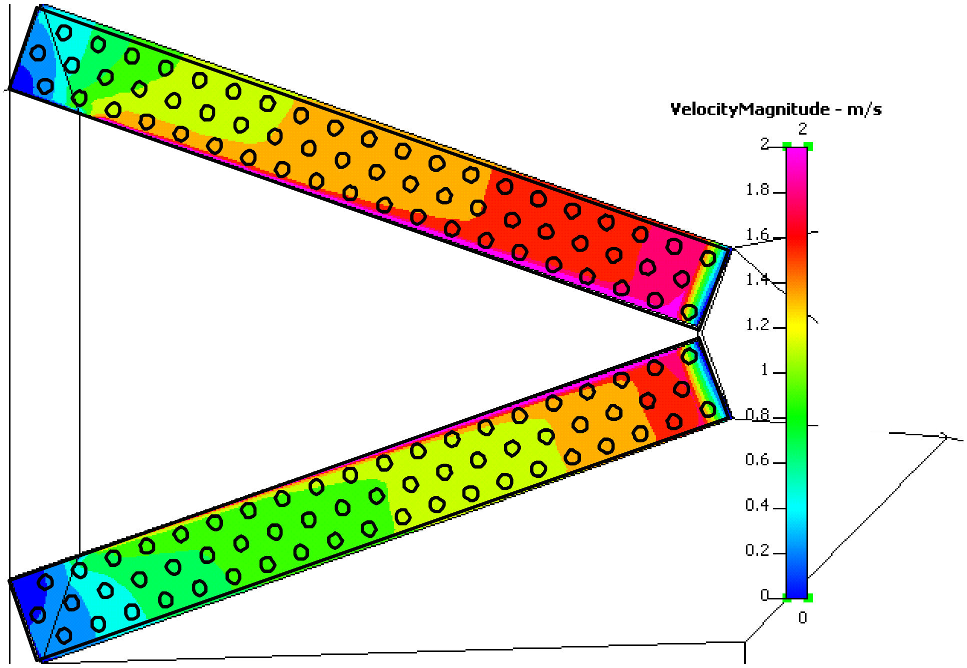

Figure 4.16 Map of velocity magnitude for 1200 CFM wet coil, Test 3

4.5 Wet Coil Reduced Flow Test Case: 0.425 m^3s^{-1} (900 CFM), Test 4

The last simulation was performed using the low flow boundary conditions and the wet coil momentum resistance coefficients. The results of the inlet velocity profile for the upper and lower slabs are shown in Figures 4.17 and 4.18, respectively. The PIV data were taken at upstream distances between 5 mm and 10 mm from the coil surface on the upper slab, and between 9 mm and 15 mm on the lower slab. Again, this model seems to predict the flow inlet rather well, with the exception that it overpredicts the velocity in the vicinity of the apex. The simulated data at 10 mm upstream matched the upper slab PIV data within ±20 % over 84 % of the coil, and the lower slab simulated data at 15 mm upstream matched the PIV data within ±20 % over 88 % of the coil. Figure 4.19 shows the velocity magnitude map for the 900 CFM wet coil test case.

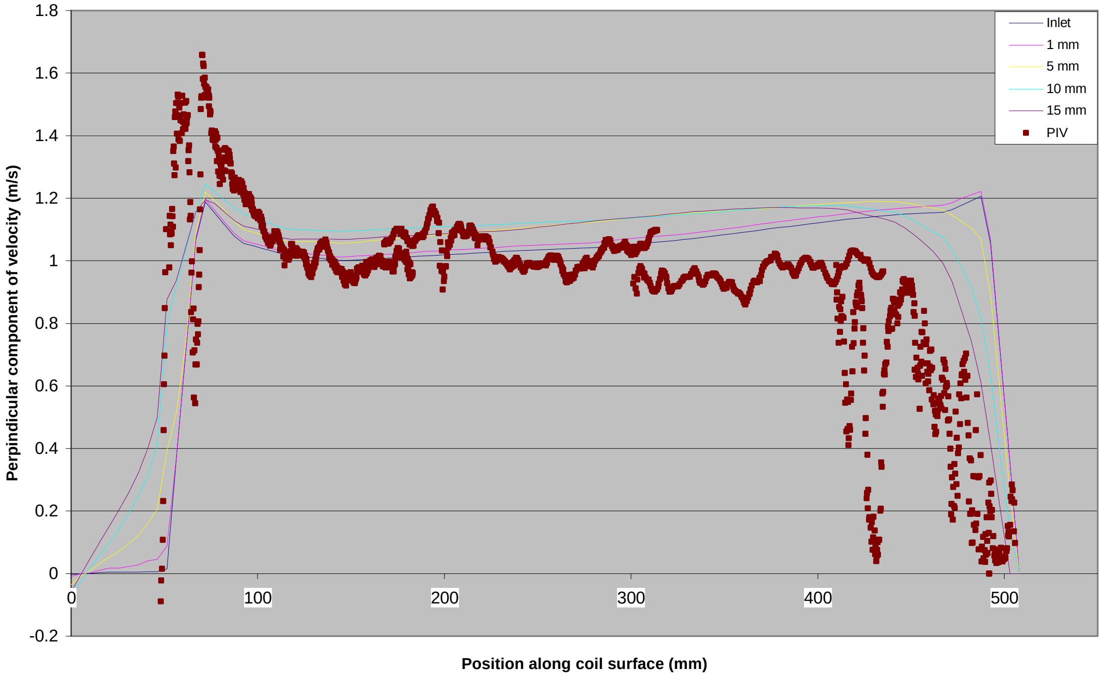

Figure 4.17 PIV and CFD data for inlet to upper slab at 900 CFM wet coil, Test 4a

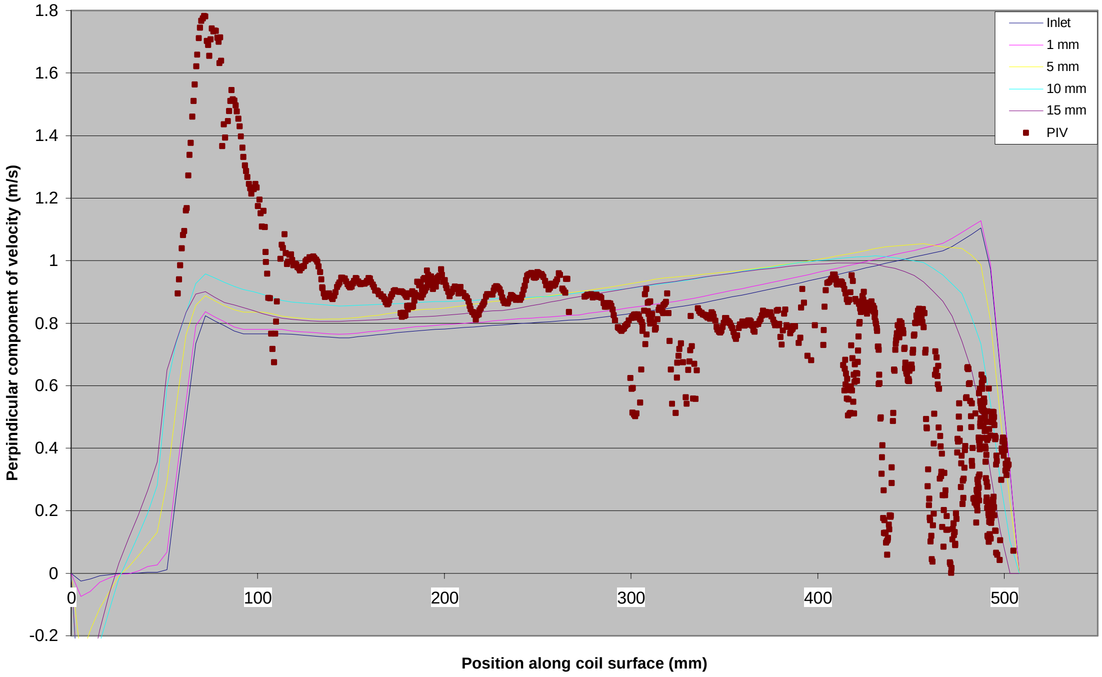

Figure 4.18 PIV and CFD data for inlet to lower slab at 900 CFM wet coil, Test 4b

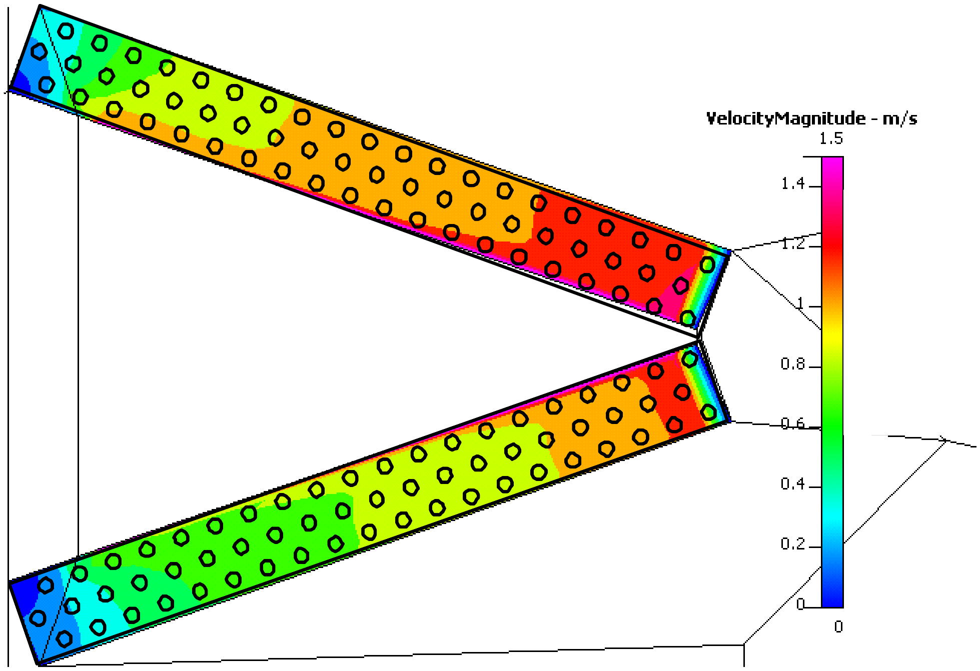

Figure 4.19 Map of velocity magnitude for 900 CFM wet coil, Test 4

4.6 Final Comments on Momentum Resistance CFD Approach

The CFD model used in this approach was built upon the premises that the coils can be modeled as a homogeneous flow resistive domain within the duct. The momentum resistance models were based on measured laboratory data of air side pressure drop through the heat exchanger versus flow rate. This approach resulted in simulations that adequately matched the measured data over large portions of the heat exchanger. Some discrepancies between the measured and simulated data were obtained in areas of expected high velocity gradients due to geometric considerations.

Since a coil operating under wet conditions does not have uniformly distributed water content inside the coil, it cannot have an evenly distributed flow resistance. Therefore, this model should be considered as a first attempt to characterize flow through a wet coil.

The developed model can be used to examine the effects of air flow rate variation and fin type variation on the velocity distribution. As shown at the beginning of the low flow simulations, the model can examine the effects of flow rate variation simply by changing the inlet air velocity. Changing the fin type would affect the flow resistance model, and therefore new coefficients for each fin set would be required; however, once these were known, these can be inserted into the model. This type of approach can also be used to examine the effects of alterations to the coil geometry, but this requires the development of a new computational domain to match that of the proposed design.

5. SUMMARY

We measured the velocity distribution of air flowing towards and from a residential A-shaped finned-tube heat exchanger using Particle Image Velocimetry. We varied the volumetric flow rate and moisture content to examine their effects on the air velocity distribution. We then constructed a Computational Fluid Dynamics model of the test coil and compared our CFD results with the laboratory measurements.

PIV Measurements

Our results showed that the presence of the condensation pan caused a significant difference between the amounts of air passing through each slab. For the dry coil tests, the upper slab received approximately 18 % more air than the lower slab for both the nominal and reduced air flow rates; this is entirely due to the geometry and placement of the condensation pan since it is the only asymmetrical feature of the heat exchanger. This difference in the air flow resulted in a 22 % difference in the capacity for both dry coil test cases. The wet coil tests showed 33 % and 15 % more air going through the top slab at the rated and reduced flow rates, respectively. Two factors contributed to this slab-to-slab air flow difference: (1) the condensation pan and (2) the difference of water amount held up by the upper and lower slab. It is not possible to determine the contributions of these influences on the slab-to-slab air flow difference without determining the in-situ distribution of held water. The wet coil tests showed a difference in slab capacities of 13 % and 12 % for the rated and reduced flow rate tests, respectively.

The results for the dry coil tests showed that varying the volumetric flow rate of air changes the magnitude of the velocity, but not the velocity distribution. The wet coil results showed that there were some changes in the velocity distribution when comparing the 1200 CFM wet coil test case with the 900 CFM wet coil test case. It is likely that these differences are mainly due to the different amount of water on the coil surface at different air flow rates.

The results for the wet coil tests showed that the presence of water in the coil tended to even out the distribution of air flow for a given slab. The data suggests that the condensate present between the fins makes the coil more resistive to air flow, which lowers the relative impact on the air distribution by the geometric features necessitated by the installation configuration (e.g., mounting bracket, condensation pan, etc.).

Observed differences between the air distributions at the inlet and outlet planes indicate that the air flow through the coil is not strictly perpendicular to the slab, and that some air redistribution within the coil occurs, particularly in the coil sections close to the mounting brackets and apex.

CFD Simulations

The CFD simulations showed that the momentum resistance modeling approach works very well for dry coil simulations. The momentum resistance modeling approach did not work as well for the wet coil cases, but the predictions were still acceptable. Hence, we could rely on further examination of the CFD results to provide information for the flow inside the coil. The simulation showed a number of locations where the air flow is considerably impeded by the geometry of the fixtures in the flow path, such as the mounting bracket and the condensation pan. The tubes located in these areas are expected to underperform compared to tubes located in other sections of the coil.

The major difficulty with implementing the momentum resistance model approach on the wet coil simulations was caused by the varying levels of water concentration held in the slabs, which are affected by the moisture removal rate from the air, the position within the heat exchanger, and time. In order to more accurately apply this approach, we would need to compile a large set of data that would characterize the pressure drop through the coil at different locations, air conditions, and flow rates, which merits a separate investigation. We would also need to provide this data in a format such that the CFD solver could retrieve values for the momentum resistance coefficients based on locations, which it currently does not have the capability to do.

Coil design considerations

The data obtained in this study suggests that a number of steps can be taken to improve the performance of A-shaped coil assemblies. This study demonstrated that the coil mounting hardware and the condensation collection device may have a significant impact on the air flow distribution. Manufacturers can seek alternative designs for these components to distribute the air flow more uniformly.

Manufacturers may consider some of the following concepts to design efficient coils for the known air flow distribution:

- Producing installation-specific heat exchangers for up-flow, down-flow, horizontal-left, and horizontal-right installations. For example, a coil in the up-flow configuration would not be installed with the condensation collection device interfering with the flow to one slab; therefore each slab would realize similar air flow and should be identical. Conversely, a coil installed horizontally with the condensation collection device would have different air flow rates through each slab and therefore should use different designs for each slab.
- Refrigerant distribution control. Rather than distributing the refrigerant evenly between the slabs, manufacturers may attempt distribute the refrigerant in a manner that would result in similar refrigerant exit conditions from each slab; i.e., more refrigerant should be routed through the slab that receives more air flow.
- Optimize refrigerant circuitry design for the in-situ air distribution. Manufacturers can alter the refrigerant circuitry so that it is best matched to the air flow distribution.
- A number of tube locations were identified where very little air flow is available for heat exchange. Some of these tubes may be eliminated, which will reduce material cost to manufacturers and lower the refrigerant side pressure drop.
- Using different fin type or spacing for the different coil slabs. This method can be used to decrease the difference in the air flow distribution for increased capacity of the coil assembly.

6. REFERENCES

AMCA 1985. *ANSI/AMCA Standard 210-85. Laboratory Methods of Testing Fans for Rating.* Air Movement and Control Association. Arlington Heights, IL.

ASHRAE 1998. *ANSI/ASHRAE Standard 37. Methods of Testing for Rating Unitary Air Conditioning and Heat Pump Equipment.* American Society of Heating, Refrigerating and Air-Conditioning Engineers. Atlanta, GA.

Chwalowski, M., Didion, D.A., and Domanski, P.A., 1987. *Verification of Evaporator Computer Models and Analysis of Performance of an Evaporator Coil*, ASHRAE Transactions 95(1).

Domanski, P.A., Yashar, D.A., Kaufman, K.A. and Michalski, R.K., 2004. *An Optimized Design of Finned-Tube Evaporators Using the Learnable Evolution Model*, HVAC&R Research 10(2), 201-211.

Lemmon, E.W., Huber, M.L., McLinden, M.O., 2007. *NIST Standard Reference Database 23: Reference Fluid Thermodynamic and Transport Properties-REFPROP, Version 8.0*, National Institute of Standards and Technology, Standard Reference Data Program, Gaithersburg, MD.

Payne, W.V. and Domanski, P.A., 2003. *Potential Benefits of Smart Refrigerant Distributors* (ARTI-21CR/605-200-50-01; 196 p.).

Taylor, B.N. and Kuyatt, C.E., 1994. *Guidelines for Evaluating and Expressing the Uncertainty of NIST Measurement Results*, NIST Technical Note 1297, The National Institute of Standards and Technology, Gaithersburg, MD.

Yashar, D.A. and Cho, H.H., 2007. *Air Side Velocity Distributions in Finned Tube Heat Exchangers*, NISTIR 7274, National Institute of Standards and Technology, Gaithersburg, MD.

Appendix A: Measurement Uncertainty

A.1: PIV Measurement Uncertainty

This analysis is based on the guidelines adopted by NIST (Taylor and Kuyatt, 1994), whereas two components of uncertainty are presented: statistically based Type A uncertainty and judgment based Type B uncertainty.

A.1.1 Type A Uncertainty for PIV Measurements

Type A uncertainty is based on the variation of repeated measurement results. In this study, we obtained the steady-state components of the flow velocity by capturing many instantaneous measurements within a turbulent flow field and averaging the resultant vector fields.

We acquired between 20 and 100 image pairs for each data point so that the transient effects of turbulent flow would be dampened out and would not influence the data. We used each pair of images to compute a vector field representative of the instantaneous flow velocity distribution. We then computed the average vector length and direction for each location in the measurement field based on the computed vectors for all of the image pairs in the data set. Therefore, each computed steady-state vector within each data file was computed by averaging between 20 and 100 vectors that were captured through independent measurements. The measurement uncertainty of each vector obtained through this method is equal to the standard deviation of the measured values of that vector, σ, divided by the square root of the number of samples, N.

The software used to perform the data reduction was also used to perform the Type A uncertainty analysis. By deploying this function, the average vector and standard deviation resultant from the N image pairs was computed at every location, in every vector field. Figures A.1 and A.2 below are representative outputs of the Type A uncertainty analysis.

Each of the 43 data sets consists of several thousand vectors; therefore it is not feasible to include the uncertainty for each individual vector. The tables in this appendix show the average Type A uncertainty calculated for each data file from the results within each data set. The velocity and standard deviations reported are representative of the average values of these parameters within the areas closest to the heat exchanger, where the data was taken for the analyses in this report. Overall, the Type A measurement uncertainty was generally better than 3 %.

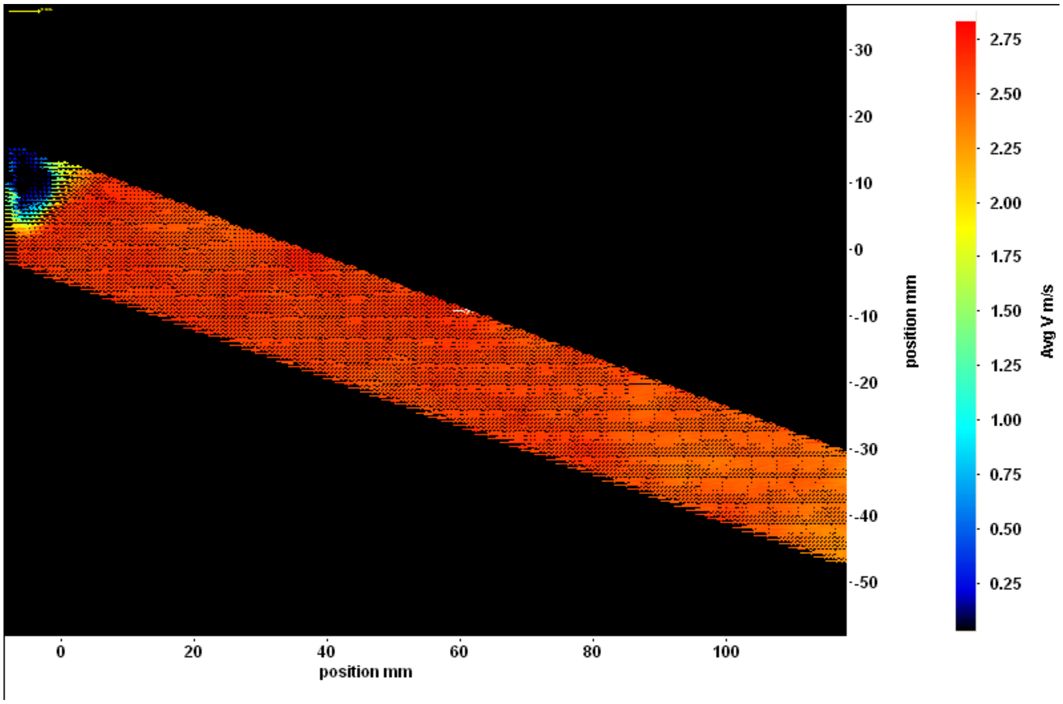

Figure A.1 Average vectors for representative flow field, based on N samples

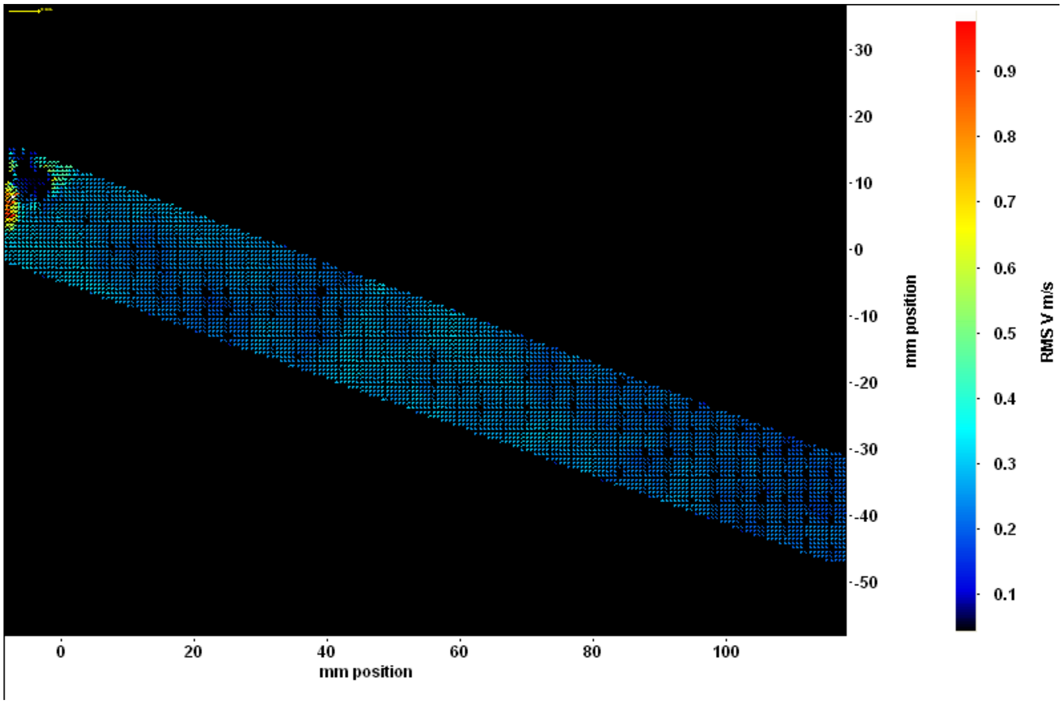

Figure A.2 Standard deviation for average vectors shown in Figure A.1

Type A Measurement Uncertainty for PIV measurements

File name	Average Velocity in Reported Region [m/s]	Average Standard Deviation in Reported Region [m/s]	Number of Samples	Average Vector Length Uncertainty [m/s]	Average Vector Length Uncertainty [%]
1200-dry-1U-exit	1.5	0.16	83	0.0176	1.1708
1200-dry-2U-exit	1.7	0.22	83	0.0241	1.4205
1200-dry-3U-exit	1.6	0.25	83	0.0274	1.7151
1200-dry-1L-exit	0.88	0.23	100	0.0230	2.6136
1200-dry-2L-exit	1.1	0.26	83	0.0285	2.5944
1200-dry-3L-exit	1.1	0.29	100	0.0290	2.6364
0900-wet-1L-inlet	2.7	0.18	50	0.0255	0.9428
0900-wet-2L-inlet	2.6	0.25	50	0.0354	1.3598
0900-wet-3L-inlet	2.5	0.23	50	0.0325	1.3011
0900-wet-4L-inlet	2.2	0.24	50	0.0339	1.5428
0900-wet-1U-inlet	2.6	0.27	50	0.0382	1.4686
0900-wet-2U-inlet	2.7	0.28	50	0.0396	1.4666
0900-wet-3U-inlet	2.6	0.24	50	0.0339	1.3054
0900-wet-4U-inlet	1.6	0.31	50	0.0438	2.7400
1200-dry-1L-inlet	3.3	0.36	20	0.0805	2.4393
1200-dry-2L-inlet	3.9	0.36	20	0.0805	2.0641
1200-dry-3L-inlet	3	0.26	20	0.0581	1.9379
1200-dry-4L-inlet	3.1	0.2	20	0.0447	1.4426
1200-dry-1U-inlet	3.4	0.33	20	0.0738	2.1703
1200-dry-2U-inlet	3.8	0.34	20	0.0760	2.0007
1200-dry-3U-inlet	3.7	0.32	20	0.0716	1.9339
1200-dry-4U-inlet	3.1	0.15	20	0.0335	1.0820
0900-dry-1L-inlet	2.6	0.32	20	0.0716	2.7521
0900-dry-2L-inlet	2.6	0.29	20	0.0648	2.4941
0900-dry-3L-inlet	2.6	0.32	20	0.0716	2.7521
0900-dry-4L-inlet	2.8	0.39	20	0.0872	3.1145
0900-dry-5L-inlet	2.6	0.27	20	0.0604	2.3221
0900-dry-6L-inlet	2	0.21	20	0.0470	2.3479
0900-dry-1U-inlet	2.9	0.24	20	0.0537	1.8505
0900-dry-2U-inlet	2.9	0.26	20	0.0581	2.0048
0900-dry-3U-inlet	2.7	0.32	20	0.0716	2.6502
0900-dry-4U-inlet	2.8	0.24	20	0.0537	1.9166
0900-dry-5U-inlet	2.7	0.25	20	0.0559	2.0704
0900-dry-6U-inlet	2.1	0.17	20	0.0380	1.8102
1200-wet-1L-inlet	3.4	0.45	20	0.1006	2.9595
1200-wet-2L-inlet	3.7	0.31	20	0.0693	1.8735
1200-wet-3L-inlet	3.4	0.35	20	0.0783	2.3018
1200-wet-4L-inlet	3.4	0.28	20	0.0626	1.8415
1200-wet-5UL-inlet	2.5	0.37	20	0.0827	3.3094
1200-wet-1U-inlet	3	0.33	20	0.0738	2.4597
1200-wet-2U-inlet	3.7	0.27	20	0.0604	1.6317
1200-wet-3U-inlet	3.5	0.33	20	0.0738	2.1083
1200-wet-4U-inlet	3.1	0.29	20	0.0648	2.0918

A.1.2 Type B Uncertainty for PIV Measurements

Type B uncertainty is based on scientific judgment of factors such as knowledge of the materials and instruments used for the measurements. The measurement uncertainty due to the pixel resolution is the only significant contributor. For this reason, we tabulated the type B uncertainty in the following table based on the pixel resolution induced measurement uncertainty. The quoted 95 % confidence uncertainty of the pixel displacement measurement was 1/10 of a pixel; therefore our uncertainty is based on the pixel size and the time difference between image pulses for each data set. The type B uncertainty has a similar magnitude to the type A uncertainty. The type B uncertainty was generally better than 2 %.

Type B Measurement Uncertainty for PIV Measurements

File Name	Pixel Size [μm]	Δt [μs]	Vector Length Uncertainty [m/s]	Average Velocity in Reported Region [m/s]	Average Vector Length Uncertainty [%]
1200-dry-1U-exit	122.3040	300	0.0408	1.5	2.7179
1200-dry-2U-exit	122.1900	300	0.0407	1.7	2.3959
1200-dry-3U-exit	122.2950	300	0.0408	1.6	2.5478
1200-dry-1L-exit	96.8212	750	0.0129	0.88	1.4670
1200-dry-2L-exit	96.5465	750	0.0129	1.1	1.1703
1200-dry-3L-exit	96.6635	750	0.0129	1.1	1.1717
0900-wet-1L-inlet	82.6651	160	0.0517	2.7	1.9135
0900-wet-2L-inlet	78.9504	160	0.0493	2.6	1.8978
0900-wet-3L-inlet	77.4652	160	0.0484	2.5	1.9366
0900-wet-4L-inlet	78.1425	160	0.0488	2.2	2.2200
0900-wet-1U-inlet	86.2217	160	0.0539	2.6	2.0726
0900-wet-2U-inlet	80.2410	160	0.0502	2.7	1.8574
0900-wet-3U-inlet	80.2842	160	0.0502	2.6	1.9299
0900-wet-4U-inlet	76.3838	160	0.0477	1.6	2.9837
1200-dry-1L-inlet	88.6643	160	0.0554	3.3	1.6792
1200-dry-2L-inlet	86.6772	160	0.0542	3.9	1.3891
1200-dry-3L-inlet	83.8982	160	0.0524	3	1.7479
1200-dry-4L-inlet	85.6739	160	0.0535	3.1	1.7273
1200-dry-1U-inlet	89.3359	160	0.0558	3.4	1.6422
1200-dry-2U-inlet	64.7136	160	0.0404	3.8	1.0644
1200-dry-3U-inlet	73.7680	160	0.0461	3.7	1.2461
1200-dry-4U-inlet	85.8033	160	0.0536	3.1	1.7299
0900-dry-1L-inlet	51.7215	160	0.0323	2.6	1.2433
0900-dry-2L-inlet	49.2601	160	0.0308	2.6	1.1841
0900-dry-3L-inlet	50.3871	160	0.0315	2.6	1.2112
0900-dry-4L-inlet	51.0678	160	0.0319	2.8	1.1399
0900-dry-5L-inlet	48.5222	160	0.0303	2.6	1.1664
0900-dry-6L-inlet	49.9559	160	0.0312	2	1.5611
0900-dry-1U-inlet	46.9954	160	0.0294	2.9	1.0128
0900-dry-2U-inlet	44.4289	160	0.0278	2.9	0.9575
0900-dry-3U-inlet	46.3822	160	0.0290	2.7	1.0737
0900-dry-4U-inlet	51.8994	160	0.0324	2.8	1.1585
0900-dry-5U-inlet	51.6151	160	0.0323	2.7	1.1948
0900-dry-6U-inlet	47.4971	160	0.0297	2.1	1.4136
1200-wet-1L-inlet	76.5899	160	0.0479	3.4	1.4079
1200-wet-2L-inlet	65.5154	160	0.0409	3.7	1.1067
1200-wet-3L-inlet	62.0064	160	0.0388	3.4	1.1398
1200-wet-4L-inlet	56.6746	160	0.0354	3.4	1.0418
1200-wet-5UL-inlet	63.6457	160	0.0398	2.5	1.5911
1200-wet-1U-inlet	74.0492	160	0.0463	3	1.5427
1200-wet-2U-inlet	71.0419	160	0.0444	3.7	1.2000
1200-wet-3U-inlet	62.8325	160	0.0393	3.5	1.1220
1200-wet-4U-inlet	61.8536	160	0.0387	3.1	1.2470

A.1.3 Combined Uncertainty for PIV Measurements

The combined uncertainty is calculated from the type A and type B uncertainty by taking the square root of the sum of the squares of both elements. Through this analysis, the combined uncertainty for the PIV measurements is shown to be generally within the 2 % - 3 % range, with the greatest uncertainty at 4 %.

Combined Measurement Uncertainty for PIV Measurements

File Name	Average Velocity in Reported Region [m/s]	Type A Uncertainty [m/s]	Type B Uncertainty [m/s]	Combined Uncertainty [m/s]	Combined Uncertainty [%]
1200-dry-1U-exit	1.5	0.0176	0.0408	0.0444	2.9593
1200-dry-2U-exit	1.7	0.0241	0.0407	0.0474	2.7853
1200-dry-3U-exit	1.6	0.0274	0.0408	0.0491	3.0713
1200-dry-1L-exit	0.88	0.0230	0.0129	0.0264	2.9972
1200-dry-2L-exit	1.1	0.0285	0.0129	0.0313	2.8461
1200-dry-3L-exit	1.1	0.0290	0.0129	0.0317	2.8850
0900-wet-1L-inlet	2.7	0.0255	0.0517	0.0576	2.1332
0900-wet-2L-inlet	2.6	0.0354	0.0493	0.0607	2.3347
0900-wet-3L-inlet	2.5	0.0325	0.0484	0.0583	2.3331
0900-wet-4L-inlet	2.2	0.0339	0.0488	0.0595	2.7034
0900-wet-1U-inlet	2.6	0.0382	0.0539	0.0660	2.5402
0900-wet-2U-inlet	2.7	0.0396	0.0502	0.0639	2.3666
0900-wet-3U-inlet	2.6	0.0339	0.0502	0.0606	2.3300
0900-wet-4U-inlet	1.6	0.0438	0.0477	0.0648	4.0510
1200-dry-1L-inlet	3.3	0.0805	0.0554	0.0977	2.9615
1200-dry-2L-inlet	3.9	0.0805	0.0542	0.0970	2.4879
1200-dry-3L-inlet	3	0.0581	0.0524	0.0783	2.6097
1200-dry-4L-inlet	3.1	0.0447	0.0535	0.0698	2.2505
1200-dry-1U-inlet	3.4	0.0738	0.0558	0.0925	2.7216
1200-dry-2U-inlet	3.8	0.0760	0.0404	0.0861	2.2662
1200-dry-3U-inlet	3.7	0.0716	0.0461	0.0851	2.3006
1200-dry-4U-inlet	3.1	0.0335	0.0536	0.0633	2.0404
0900-dry-1L-inlet	2.6	0.0716	0.0323	0.0785	3.0199
0900-dry-2L-inlet	2.6	0.0648	0.0308	0.0718	2.7609
0900-dry-3L-inlet	2.6	0.0716	0.0315	0.0782	3.0068
0900-dry-4L-inlet	2.8	0.0872	0.0319	0.0929	3.3166
0900-dry-5L-inlet	2.6	0.0604	0.0303	0.0676	2.5986
0900-dry-6L-inlet	2	0.0470	0.0312	0.0564	2.8195
0900-dry-1U-inlet	2.9	0.0537	0.0294	0.0612	2.1096
0900-dry-2U-inlet	2.9	0.0581	0.0278	0.0644	2.2217
0900-dry-3U-inlet	2.7	0.0716	0.0290	0.0772	2.8594
0900-dry-4U-inlet	2.8	0.0537	0.0324	0.0627	2.2395
0900-dry-5U-inlet	2.7	0.0559	0.0323	0.0645	2.3904
0900-dry-6U-inlet	2.1	0.0380	0.0297	0.0482	2.2967
1200-wet-1L-inlet	3.4	0.1006	0.0479	0.1114	3.2773
1200-wet-2L-inlet	3.7	0.0693	0.0409	0.0805	2.1759
1200-wet-3L-inlet	3.4	0.0783	0.0388	0.0873	2.5686
1200-wet-4L-inlet	3.4	0.0626	0.0354	0.0719	2.1157
1200-wet-5UL-inlet	2.5	0.0827	0.0398	0.0918	3.6720
1200-wet-1U-inlet	3	0.0738	0.0463	0.0871	2.9034
1200-wet-2U-inlet	3.7	0.0604	0.0444	0.0749	2.0255
1200-wet-3U-inlet	3.5	0.0738	0.0393	0.0836	2.3883
1200-wet-4U-inlet	3.1	0.0648	0.0387	0.0755	2.4353

A.2 Measurement Uncertainty for Air Flow Reported Values

Temperature, Humidity, and Flow Rate of Air

A.2.1 Type A Uncertainty for Air Flow Reported Values

Type A uncertainty is based on the variation of repeated measurement results. In this study, we scanned the air temperatures, dew point temperature, and volumetric flow rate every 16 seconds; therefore the Type A uncertainty is based on a very large number of data points taken every 16 seconds over the entire test duration. The air flow data sets were taken for each set of conditions on each day; therefore each air flow data set encompasses an entire set of PIV scans. The computed steady-state value for each reported measurement was the average of during the test duration and the uncertainty is equal to the standard deviation of the measured values of that vector, σ, divided by the square root of the number of samples, N.

Type A Measurement Uncertainty for Air Flow Measurements

File name	N scans	Air inlet temp [C]	σ[C]	U_{Tair} [C]	Dew point temp [C]	σ [C]	U_{Tdp} [C]	Flow rate [CFM]	σ [CFM]	U_Q [CFM]
1200 dry inlet	1533	26.69	0.432	0.011	4.082	0.35	0.009	1194.11	3.18	0.08
1200 wet inlet	1172	26.66	0.093	0.003	15.91	0.14	0.004	1204	2.26	0.07
900 dry inlet	1156	26.75	0.047	0.001	1.81	0.19	0.006	900.40	1.92	0.06
900 wet inlet	411	26.74	0.018	0.001	15.66	0.06	0.003	893.98	1.72	0.08
1200 dry exit upper	939	26.93	0.129	0.004	4.08	0.34	0.011	1201.11	3.17	0.10
1200 dry exit lower	794	26.61	0.285	0.010	-3.53	0.46	0.016	1205.42	2.7859	0.10

A.2.2 Type B Uncertainty for Air Flow Reported Values

Temperature Measurements

All of the temperature measurements performed for these tests were determined by thermocouples. Their voltage signals were measured with the data acquisition system and then converted into a temperature.

The equation used in the test rig's control program to convert the voltage signals into temperatures was a sixth degree polynomial of the form:

$$T = f(V) = (A + B\,V + C V^2 + D\,V^3 + E\,V^4 + F\,V^5 + G\,V^6) \tag{A.1}$$

where:

T = temperature (°C)
V = measured voltage (µV)

The uncertainty in the temperature measurements is therefore related to the voltage by:

$$\frac{\partial T}{\partial V} = \left(B + 2C\,V + 3D\,V^2 + 4E\,V^3 + 5F\,V^4 + 6G\,V^5\right) \tag{A.2}$$

According to the manufacturer of the datalogger voltmeter, the 95 % uncertainty of the voltage measurement (*VM*) was: $E_{VM} = dV\left(VM\right) = \pm\ 0.007\ \%\ of\ \ reading +\ 5\ \mu V$.

The measurement of a temperature actually is the measurement of the difference to a reference temperature. The data acquisition system provided a temperature compensation to 0 °C with a given uncertainty of: E_{TC} = dTC = ± 0.2236 °C.

Therefore the uncertainty of the measurement of absolute temperature gives:

$$E_{\mathrm{T}} = \sqrt{\left(\frac{\partial T}{\partial V}\ dVM\right)^2 + \left(dTC\right)^2} \tag{A.3}$$

In addition to the common thermocouple measurements, the dew-point temperature in the air duct was measured to evaluate the humidity ratio of the moist air in the duct.

The manufacturer of the dew-point hygrometer specified the 95 % uncertainty in this measurement to be: $E_{T_{\mathrm{dew}}} = dT_{\mathrm{dew}} = \pm\ 0.05\ \%\ of\ \ reading.$

Air Flow Rate

The air flow test chamber was built according to ANSI/AMCA 210-1985. According to this standard, the air flow rate Q is given by:

$$\dot{\forall} = 1.0544Y\left[\frac{\Delta p_{\mathrm{n}}}{\rho_{\mathrm{n}}}\right]^{1/2} \Sigma\left(CA\right) \qquad \text{(A.4)}$$

where:

Y = expansion factor (assumed constant at 0.96)
Δp_{n} = static pressure drop across nozzle, kPa
ρ_{n} = density of the moist air just upstream of nozzles, kg/m^3
A = nozzle throat area, m^2
C = discharge coefficient (assumed constant at 0.95)

The setup was built with four nozzles set in parallel within the air flow chamber; the diameters of these nozzles are 0.1007 m, 0.1005 m, 0.1015 m, and 0.0764 m and their measurement uncertainty has a negligible impact on the above equation.

The partial derivatives required for the uncertainty analysis of Q are therefore:

$$\frac{\partial\dot{\forall}}{\partial\Delta p_{\mathrm{n}}} = 0.5272Y\left[\frac{1}{\rho_{\mathrm{n}}\Delta p_{\mathrm{n}}}\right]^{1/2} \Sigma\left(CA\right) \qquad \text{(A.5)}$$

$$\frac{\partial\dot{\forall}}{\partial\rho_{\mathrm{n}}} = -0.5272Y\left[\frac{\Delta p_{\mathrm{n}}}{\rho^{3}_{n}}\right]^{1/2} \Sigma\left(CA\right) \qquad \text{(A.6)}$$

Using the above partial derivatives we get the uncertainty as follows:

$$E_{\dot{\forall}} = \left[\left(\frac{\partial\dot{\forall}}{\partial\Delta p_{\mathrm{n}}}\, d\Delta p_{\mathrm{n}}\right)^2 + \left(\frac{\partial\dot{\forall}}{\partial\rho_{n}}\, d\rho_{n}\right)^2\right]^{1/2} \qquad \text{(A.7)}$$

The uncertainty of the pressure difference across the nozzle was taken from the sensor manufacturer data as ±2.4409 Pascals at 95 % confidence.

Next, the uncertainty in the moist air's density ρ_n had to be evaluated. The density was calculated using the ideal gas equation and the humidity ratio.

$$\rho_n = \frac{p_{\mathrm{n}}(1+\omega)}{RT\ (1+1.6078\ \omega)} \tag{A.8}$$

where:

The factor 1.6078 is the ratio of the molar weights of air and water.
R is the universal gas constant
T is the temperature of air entering the nozzle
ω is the humidity ratio.

Through the duration of all of the tests in this study, the humidity ratio was maintained within the range of $0.004 \le \omega \le 0.011$. Over this small range, the extreme values show that the humidity's influence on the calculated density is very small, only showing up in the fourth significant digit; therefore, we can neglect the partial derivative of density with respect to the humidity ratio.

The partial derivatives of interest are:

$$\frac{\partial \rho_n}{\partial p_{\mathrm{n}}} = \frac{(1+\omega)}{R\,T\,(1+1.6078\,\omega)} \tag{A.9}$$

Plugging in the specified values for w, R, and T, we can see that $\frac{\partial \rho_n}{\partial p_{\mathrm{n}}}$ is $0.00001155\frac{\mathrm{s}^2}{\mathrm{m}^2}$ for low humidity test cases and $0.00001150\frac{\mathrm{s}^2}{\mathrm{m}^2}$ for the high humidity test cases.

$$\frac{\partial \rho_5}{\partial T} = \frac{-p_{\mathrm{n}}(1+\omega)}{R\,T^2(1+1.6078\,\omega)} \tag{A.10}$$

Plugging in the specified values for w, R, and T, we can see that $\frac{\partial \rho_n}{\partial T}$ is $-0.00386\frac{\mathrm{kg}}{\mathrm{m}^3\mathrm{K}}$ for low humidity test cases and $-0.00385\frac{\mathrm{kg}}{\mathrm{m}^3\mathrm{K}}$ for the high humidity test cases.

The measurement is therefore:

$$E_{\rho_5} = \left[\left(\frac{\partial \rho_5}{\partial \mathrm{p_n}}\,dp_{\mathrm{n}}\right)^2 + \left(\frac{\partial \rho_5}{\partial T}\,dT\right)^2\right] \tag{A.11}$$

In all cases studied, the uncertainty of the measured density based on the uncertainty of the measured pressure and temperature is $0.001\frac{\mathrm{kg}}{\mathrm{m}^3}$.

Type B Measurement Uncertainty for Air Flow Measurements						
File Name	ΔP_n $[\frac{\text{kg}}{\text{ms}^2}]$	ρ_5 $[\frac{\text{kg}}{\text{m}^3}]$	$\frac{\partial\dot{\forall}}{\partial\Delta P}$ $[\frac{\text{m}^4\text{s}}{\text{kg}}]$	$\frac{\partial\dot{\forall}}{\partial\rho}$ $[\frac{\text{m}^6}{\text{kg}\cdot\text{s}}]$	U $\dot{\forall}$ $[\frac{\text{m}^3}{\text{s}}]$	U $\dot{\forall}$ [CFM]
1200 dry inlet	241.83	1.2208	0.000799	0.1584	0.00196	4.15
1200 wet inlet	246.36	1.2108	0.000796	0.1618	0.00195	4.13
900 dry inlet	138.43	1.2238	0.00106	0.1194	0.00259	5.49
900 wet inlet	140.36	1.2137	0.00105	0.1217	0.00257	5.45
1200 dry exit upper	244.86	1.2207	0.000795	0.1594	0.00195	4.13
1200 dry exit lower	242.78	1.2198	0.000795	0.1598	0.00195	4.13

A.2.3 Combined Uncertainty for Air Flow Reported Values

Combined Measurement Uncertainty for Air Flow Measurements					
File Name	Reported Flow Rate $[\frac{m^3}{s}]$	Type A Uncertainty $[\frac{m^3}{s}]$	Type B Uncertainty $[\frac{m^3}{s}]$	Combined Uncertainty $[\frac{m^3}{s}]$	Combined Uncertainty [%]
1200 dry inlet	0.5636	0.00004	0.00196	0.00196	3.48
1200 wet inlet	0.5682	0.00003	0.00195	0.00195	3.43
900 dry inlet	0.4249	0.00003	0.00259	0.00259	6.10
900 wet inlet	0.4219	0.00004	0.00257	0.00257	6.06
1200 dry exit-upper	0.5669	0.00005	0.00195	0.00195	3.42
1200 dry exit-upper	0.5689	0.00005	0.00195	0.00195	3.43

A.3 Measurement Uncertainty for Water Side Capacity

When measuring the water side capacity, the data logger was continuously running throughout the duration of the measurements, scanning the channels every 30 seconds. Because of this, just as was the case for the parameters calculated in the previous section, the Type A component of uncertainty was deemed insignificant when compared to the Type B uncertainty.

The heat capacity was calculated for each slab of the coil during the measurements using the water enthalpy method. Chilled water was fed to the apex of the heat exchanger, and the water exiting each slab was passed through a floating bob meter. The meters were outfitted with flow controlling valves, which were used to balance the flow of water through each slab. In all test cases the valves were set such that the floating bob meters read the same flow rate of water. The floating bob meters were graduated with divisions of 0.5 gallons per minute, and could be read to within 0.1 gallons per minute. Using the density of water as $1000\ \frac{\mathrm{kg}}{\mathrm{m}^3}$, we can convert this to an accuracy in mass flow rate of $\pm 6.3\ \frac{\mathrm{g}}{\mathrm{s}}$. The water flowing though the upper slab was also piped through a coriolis mass flow meter, which was calibrated to $0.03\ \frac{\mathrm{g}}{\mathrm{s}}$ over the range of 0 to $300\ \frac{\mathrm{g}}{\mathrm{s}}$. Therefore, the uncertainty on the lower slab is based on the floating bob flow meter, and the uncertainty on the upper slab is based on the coriolis flow meter. The temperature difference experienced by the water through each slab was measured using a 5 junction thermopile inserted into an oil filled well; each thermopile was calibrated to 0.1 ºC. The following equation was used to calculate the heat capacity for each slab:

$$Q = \dot{m} C_p \Delta T$$

The partial derivatives with respect to the measured quantities are:

$$\frac{\partial Q}{\partial \dot{m}} = C_p \Delta T$$

and

$$\frac{\partial Q}{\partial \Delta T} = \dot{m} C_p$$

The Type B measurement uncertainty shown in the table is equivalent to the total measurement uncertainty.

Type B Measurement Uncertainty for Water Side Capacity Measurements						
	Bottom slab			Top Slab		
File Name	$\frac{\partial Q}{\partial \dot{m}}\ [\frac{\mathrm{J}}{\mathrm{g}}]$	$\frac{\partial Q}{\partial \Delta T}\ [\frac{\mathrm{W}}{\mathrm{K}}]$	U_Q [W]	$\frac{\partial Q}{\partial \dot{m}}\ [\frac{\mathrm{J}}{\mathrm{g}}]$	$\frac{\partial Q}{\partial \Delta T}\ [\frac{\mathrm{W}}{\mathrm{K}}]$	U_Q [W]
1200 dry inlet	15.9	1192	169.8	19.2	1192	35.8
1200 wet inlet	21.8	1197	196.3	24.7	1197	119.7
900 dry inlet	13.0	1188	153.8	15.5	1188	118.8
900 wet inlet	19.2	1192	179.5	21.3	1192	119.2
1200 dry exit upper	15.5	1188	169.5	19.2	1188	118.8
1200 dry exit lower	15.8	1194	168.2	18.8	1194	119.5

Appendix B: Coordinates Used for CFD Model

Coordinates for CFD Model		
Point	x-coordinate [mm]	y-coordinate [mm]
A	0.000	0.000
B	0.000	508.000
C	965.200	0.000
D	965.200	73.025
E	965.200	434.975
F	965.200	508.000
G	1006.969	88.228
H	1006.969	419.772
I	986.918	13.355
J	986.918	494.645
K	986.918	508.000
L	1442.564	246.771
M	1442.564	261.229
N	1464.282	187.101
O	1464.282	320.899
P	1466.850	38.100
Q	1466.850	0.000
R	1447.800	254.000
S	1600.200	184.150
T	2438.400	508.000
U	2438.400	0.000
V	976.059	43.190
W	976.059	464.810

Appendix C: Pressure Drop Data Used for Momentum Resistance Models

Data Used to Determine Momentum Resistance Coefficients for Dry Coil			
Flow Rate Through Lower Coil $[\frac{m^3}{s}]$	Pressure Drop $[\frac{N}{m^2}]$	Average Velocity $[\frac{m}{s}]$	Pressure Gradient $[\frac{Pa}{m}]$
0.1740	11.6325	0.7491	183.1882
0.2881	31.2607	1.2404	492.2938
0.2574	21.6707	1.1084	341.2714
0.2177	17.2619	0.9375	271.8403
0.1888	13.7248	0.8128	216.1386
0.2400	20.3007	1.0335	319.6968

Data used to Determine Momentum Resistance Coefficients for Wet Coil			
Flow Rate Through Lower Coil $[\frac{m^3}{s}]$	Pressure Drop $[\frac{N}{m^2}]$	Average Velocity $[\frac{m}{s}]$	Pressure Gradient $[\frac{Pa}{m}]$
0.1826	30.9377	0.7864	487.2085
0.2435	38.9261	1.0485	613.0098